

Prepared for:
ONR/NRL

Modeling of mud-wave interaction

Mud-induced wave transport & wave-induced mud transport

Report

November 2007

Prepared for:

ONR/NRL

Modeling of mud-wave interaction

Mud-induced wave transport & wave-induced mud transport

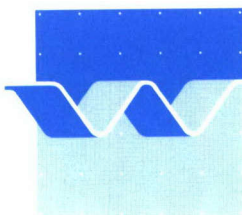
Johan C. Winterwerp

20071219026

Report

November 2007

DISTRIBUTION STATEMENT A
Approved for Public Release
Distribution Unlimited



wL | delft hydraulics

REPORT DOCUMENTATION PAGE

Form Approved
OMB No. 0704-0188

The public reporting burden for this collection of information is estimated to average 1 hour per response, including the time for reviewing instructions, searching existing data sources, gathering and maintaining the data needed, and completing and reviewing the collection of information. Send comments regarding this burden estimate or any other aspect of this collection of information, including suggestions for reducing the burden, to Department of Defense, Washington Headquarters Services, Directorate for Information Operations and Reports (0704-0188), 1215 Jefferson Davis Highway, Suite 1204, Arlington, VA 22202-4302. Respondents should be aware that notwithstanding any other provision of law, no person shall be subject to any penalty for failing to comply with a collection of information if it does not display a currently valid OMB control number.

PLEASE DO NOT RETURN YOUR FORM TO THE ABOVE ADDRESS.

1. REPORT DATE (DD-MM-YYYY)

31/12/2006

2. REPORT TYPE

final

3. DATES COVERED (From - To)

15/03/2005-31/12/2006

4. TITLE AND SUBTITLE

Modeling of mud-wave interaction:
Mud-induced wave transport & wave-induced mud transport

Implementation in Delft3D

5a. CONTRACT NUMBER

N00014-05-1-0484

5b. GRANT NUMBER

5c. PROGRAM ELEMENT NUMBER

6. AUTHOR(S)

Johan C. Winterwerp

5d. PROJECT NUMBER

5e. TASK NUMBER

5f. WORK UNIT NUMBER

7. PERFORMING ORGANIZATION NAME(S) AND ADDRESS(ES)

Delft Hydraulics
PO Box 166, 2600 MH, Delft
The Netherlands

8. PERFORMING ORGANIZATION
REPORT NUMBER

Z3672

9. SPONSORING/MONITORING AGENCY NAME(S) AND ADDRESS(ES)

Office of Naval Research
Ballston Centre Tower One
800 North Quincy Street
Arlington VA 22217-5660, USA

10. SPONSOR/MONITOR'S ACRONYM(S)

ONR

11. SPONSOR/MONITOR'S REPORT
NUMBER(S)

12. DISTRIBUTION/AVAILABILITY STATEMENT

unlimited availability

13. SUPPLEMENTARY NOTES

14. ABSTRACT

This report describes the set-up and mathematical-physical formulations of a model simulating the interaction between soft mud deposits and waves. This model presumes a two-layer schematization, the lower layer consisting of liquefiable mud of high density and viscosity, and the upper layer of low viscous water. From an analytical solution of the 2L schematization the dispersion relation for the wave propagation and attenuation is derived, which can be re-written in the form of an energy dissipation term, implemented in SWAN (Delft3D-wave). Next, the radiation stresses are elaborated and added to the 2L schematization to account for wave-induced mud transport. Also a new rheological model has been proposed to describe liquefaction of soft mud by waves, and the subsequent strength recovery after the passage of the waves. A scheme is presented on how to implement these formulations in Delft3D.

15. SUBJECT TERMS

fluid mud, wave damping, wave-induced mud transport, rheology, Delft3D, SWAN

16. SECURITY CLASSIFICATION OF:

a. REPORT

U

b. ABSTRACT

U

c. THIS PAGE

U

17. LIMITATION OF
ABSTRACT

SAR

18. NUMBER
OF
PAGES

63

19a. NAME OF RESPONSIBLE PERSON

Johan C. Winterwerp

19b. TELEPHONE NUMBER (Include area code)

+31-15-2858813

Contents

1	Introduction.....	1-1
2	Set up the model.....	2-1
3	Model development.....	3-1
3.1	The 2L FLUID MUD MODEL.....	3-1
3.2	Modeling water-bed exchange processes.....	3-4
3.3	Mud-induced wave-damping.....	3-6
3.4	Wave-induced mud transport.....	3-12
3.5	A criterion for liquefaction of the mud bed	3-15
3.6	Strength evolution and the rheological model	3-22
4	Implementation into the 2L FLUID MUD MODEL.....	4-1
5	Application mud-induced wave damping	5-1
5.1	Validation against laboratory experiments.....	5-1
5.2	Application to Guyana coast.....	5-2
5.2.1	Observations	5-2
5.2.2	Simulations	5-5
6	Application of wave-induced mud transport.....	6-1
7	Application of wave-induced liquefaction	7-1
8	References.....	8-1
Appendices		
A	Appendix: List of symbols	A-1
B	.Appendix: Table of parameters	B-1

I Introduction

Muddy coasts are found throughout the world (e.g. Healy et al., 2002). Some of these coasts are characterized by permanent extensive thick mud deposits, covering part of the hinterland (coastal plain) as well, as in the larger Mississippi delta, including Louisiana coastal system, and the larger Amazon delta, including the Guiana's. Elsewhere the mud deposits are found predominantly offshore, as in Kerala, India; at some locations migrating to the shore occasionally, as at Cassino Beach, Brazil.

A spectacular phenomenon occurring in muddy coastal systems is the damping of incoming waves, sometimes to a degree that locally completely still water zones are formed (e.g. Gade, 1958; Kurup, 1972). For instance, Tubman and Suhayda (1976) carried out measurements in 1976 in the East Bay near the Mississippi mouth at two stations at 20 and 3.5 m water depth and 3.5 km apart. The bed consists of thick layers (several 10 m) of soft mud with a strength close to the liquid limit (1.75 – 2.36 kPa). From a simple estimation of the wave damping to be expected by bed friction only, they concluded that the wave height was dissipated within the soft mud by about 50% over this 3.5 km trajectory.

Recently, Sheremet and Stone (2003) analyzed five day wave measurements in early 2001 at two stations located at the 5 m isobath in the larger Atchafalaya Bay. One station was located above a sandy seabed, and the other over a muddy seabed. Though these stations were 150 km apart, the local bathymetry, incoming wave conditions and local wind climate were so similar that a comparison of wave heights at these stations is meaningful. They observed considerably lower wave heights (more than 70% smaller) at the muddy site in comparison to the observations at the sandy site. This damping of wave height is again attributed to dissipation of wave energy in the mud layers. Moreover, they observed wave damping throughout the entire energy spectrum, which is unexpected as one would expect that the smaller waves would not be affected as much by the muddy seabed.

Wells and Kemp (1986) measured wave heights in the coastal area of Surinam at three stations at 7.1, 4.7 and 3.1 m water depth approximately 21.1, 11.7 and 4.3 km off the coast, respectively. This coastal area is characterized by thick layers of Amazon mud (thickness exceeding a few 100 m). They observed 88% and 96% dissipation of the wave energy traveling from the most seaward monitoring station towards the shore. It is noted that also in this case dissipation over the entire energy spectrum was observed, though the longer waves dissipated most.

Conceptually, wave damping over muddy beds is characterized by a sequence of events. First, small elastic deformations are generated within the muddy seabed by the cyclical stresses induced by incoming waves. At a moment, these stresses may exceed the strength of the bed, and internal failure occurs resulting in liquefaction of (part of) the seabed. This can be a fairly rapid process (i.e. of the order of tens of seconds, up to a few minutes at most, e.g. Foda and Zhang (1994); Lindenberg et al., (1989)), but this is not always the case. The bed can then be characterized as fluid mud. The incoming waves now generate internal waves at the mud-water interface, which are dissipated by internal friction within the fluid mud layer. More sediment may liquefy below this fluid mud layer, but this is not likely because of two reasons:

- the fluid mud layer damps the waves, hence the stresses within the bed,
- earlier events (stress history) will limit the thickness of the bed that is sensitive to liquefaction.

Hence, one may infer that the (maximum) thickness of the liquefiable bed is a characteristic feature of a specific coastal system. This thickness is determined by the mud properties and the wave climate, which together also determine the important stress history. Moreover, erosion (entrainment) of the mud layer may occur and has to be accounted for on a somewhat larger time scale.

The waves also induce horizontal stresses on the (fluid) mud layer, known as radiation stresses. Hence, the fluid mud may move under the influence of waves, provided that the stresses exceed the strength of the mud. If the mud cannot move, for instance when it is attached to the shore, some set-up may occur as under normal wave conditions; however, no data are available at present.

After passage of waves, the liquefied mud will completely or partly regain its strength. As the mud has a very low permeability, liquefaction, wave damping, mud transport and strength recovery take place under more or less undrained conditions, and the density of the mud (water content) remains fairly constant.

In this report the development of a hydro-sedimentological model is proposed, which contains the entire wave-mud cycle, i.e.:

1. Liquefaction of a muddy seabed by incoming waves during storm conditions,
2. Damping of waves by the liquefied mud,
3. Movement of the liquefied mud by the waves,
4. Strength recovery of the muddy seabed after passage of the storm.

Section 2 describes the set-up of this model and the rationale behind the various choices that have been made. The physical-mathematical description of the various modules and their implementation are presented in Section 3 and 4. Section 5 through 7 describe results of the model simulations on the mud behavior at Guyana coast and at Cassino Beach. In Section 8 the results are summarized and discussed and recommendations for further developments and testing are given.

2 Set up the model

We focus on the behavior of fairly old (i.e. years, but not centuries or more), non-consolidating mud deposits, which liquefy frequently, i.e. of the order of once a year or more often. The strength of these mud layers under quiescent conditions is of the order of the Liquid Limit, or a bit larger. We do not consider very old and stable geological deposits, as encountered on the continental shelf. This implies that liquefaction is a fairly rapid process, i.e. liquefaction takes place in several 10 – 100 wave cycles, and not in many 1,000 to 10,000 characteristic for said geological deposits.

We also do not deal with very recent, soft deposits, so that strength recovery after the wave events takes place without significant consolidation. This implies that the entire wave-mud cycle takes place under undrained conditions, and that the dry density (water content) of the mud remains constant.

We further assume that the mud deposits are more or less homogeneous, not containing (thick) layers of sand or of other sediment. Furthermore, our approach will be limited to situations where the thickness of the liquefiable mud layers are small in comparison to the water depth, so that the water movement itself is not largely affected by the behavior of the mud layers, apart from a reduced interfacial friction.

These assumptions imply that the wave-mud cycle can be modeled with a two-layer approach, as the interface between the liquefied mud layer and the overlying water column will be very stable because of the large density difference between the two fluids.

The effect of viscous wave damping over fluid mud will be implemented in SWAN. This model requires input of the thickness, extension, density and viscosity of the fluid mud layer, and of course information on bathymetry, incoming waves and wind stresses to compute locally generated waves. The important feed-back between incoming waves and the mud bed (liquefaction, damping, traction, consolidation) has not yet been accounted for. We propose to model liquefaction of the fluid mud, its movement and the consolidation after the wave events, and the feed-back with the waves (SWAN) within the DELFT3D-2L FLUID MUD MODEL. This model is currently incorporated as a special in the standard version of DELFT3D. A detailed description of the model can be found in the User Manual (Wang and Winterwerp, 1992) and in Winterwerp et al. (2003). This model consists of three layers (e.g. Section 3.1):

- an upper layer, the water layer, which may contain dilute suspensions of mud, and which is modeled in three dimensions,
- the depth-averaged fluid mud layer in which the sediment concentration is assumed to remain constant,
- the bed layer (consisting of sand or well-consolidated mud, which can be eroded and can store mud.

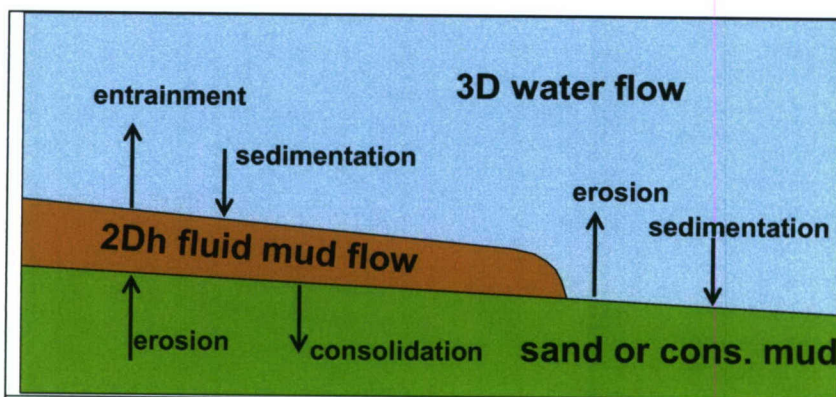


Fig. 2.1: Sediment balance in DELFT3D-2L FLUID MUD MODEL.

Fig. 2.1 presents a sketch of the mass balance of the 2L model and Fig. 2.2 presents a sketch of the momentum balance, in x -direction only for simplicity.

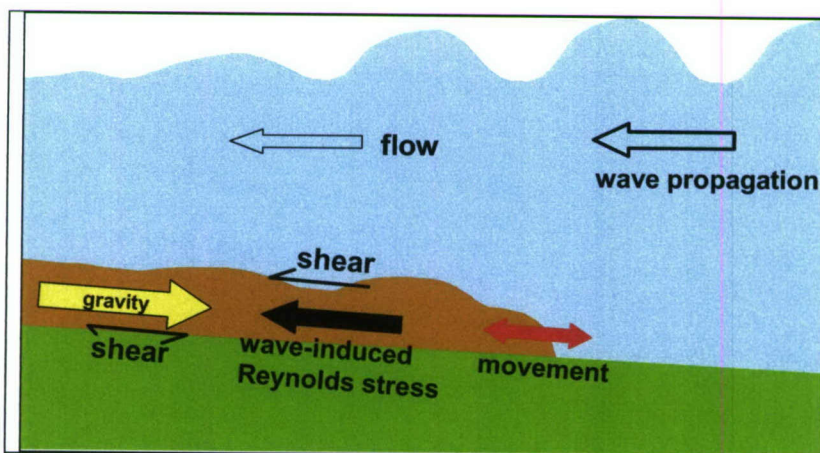


Fig. 2.2: Momentum balance in DELFT3D-2L FLUID MUD MODEL.

A detailed description of the existing DELFT3D-2L FLUID MUD MODEL is given in Section 3.1. Extension of the model will be carried out in small steps to guarantee testable sub-products, not only to test the model implementations themselves, but also the mathematical-physical concepts, as these are new to a large extent. The proposed phasing is described in Table 2.1, including reference to the sections with further details. Column 3 summarizes the material properties of the liquefied that have to be specified by the user: in Phase 1 and 2, the thickness and extension $\delta(x,y)$ of the mud layer, its viscosity μ , strength τ_B and density ρ have to be prescribed. Thickness and extension of the mud layer is modeled in Phase 3 of the model development, whereas the rheological parameters of the mud are modeled in Phase 4.

Table 2.1: Phasing of the model set-up.

Phase	physical process	for the given physical parameters	see Sections
1	mud-induced wave damping	$\delta(x,y)$, μ , τ_B , ρ_m	3.3 & 5
2	wave-induced mud transport	$\delta(x,y)$, μ , τ_B , ρ_m	3.4 & 6
3	wave-induced liquefaction	μ , τ_B , ρ_m	3.5 & 7
4	strength recovery after storm	ρ_m	3.6

3 Model development

3.1 The 2L FLUID MUD MODEL

Fig. 3.1 presents a sketch of the DELFT3D 2L FLUID MUD MODEL and the definition of the parameters used.

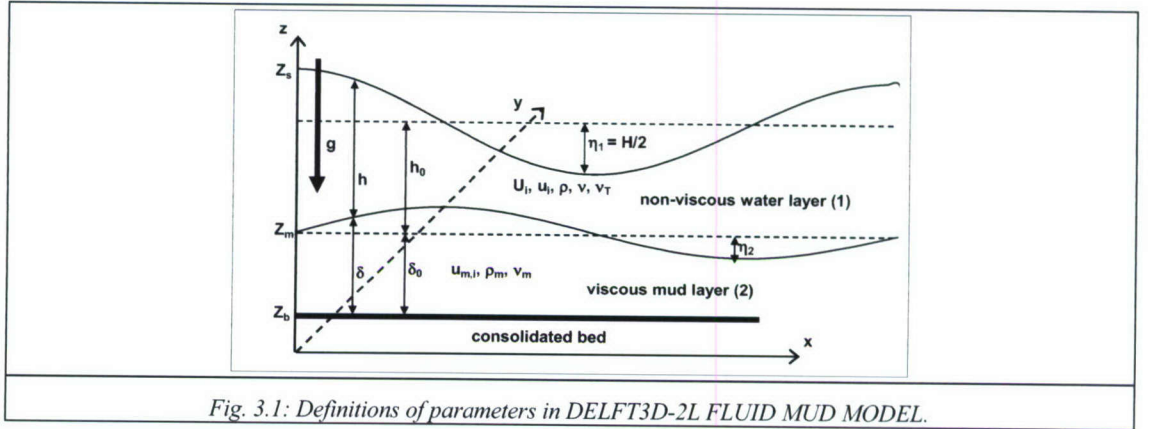


Fig. 3.1: Definitions of parameters in DELFT3D-2L FLUID MUD MODEL.

The three-dimensional water movement and sediment transport in the **upper layer**, containing dilute suspensions of mud are implemented in the 2L FLUID MUD MODEL. We assume a hydrostatic pressure distribution, simplifying the vertical momentum equation. We use Einstein's summation convention, and the continuity equation for water reads:

$$\frac{\partial u_i}{\partial x_i} = 0 \quad (i = 1, 2, 3) \quad (3.1)$$

where $u_i(x, y, z, t)$ is the three-dimensional velocity vector. The vertical velocity u_3 follows from closure of the three-dimensional continuity equation. The momentum equation reads (i & $j = 1, 2$):

$$\begin{aligned} \frac{\partial u_i}{\partial t} + u_j \frac{\partial u_i}{\partial x_j} - e_{ijk} f_k u_j + \frac{gh}{2\rho} \frac{\partial \rho}{\partial x_i} + g \frac{\partial Z_{s,i}}{\partial x_i} - \frac{\partial}{\partial x_j} (\nu + \nu_T) \frac{\partial u_i}{\partial x_j} + \\ - \frac{\tau_{Z_{s,j}}}{\rho h} \Big|_{z=Z_s} + \frac{\tau_{Z_{l,j}}}{\rho h} \Big|_{z=Z_l} = 0 \end{aligned} \quad (3.2)$$

where $i = 1, 2$ (i.e. x, y – see Fig. 3.1), e_{ijk} is the permutator, f = Coriolis parameter, Z_ℓ is either Z_m if fluid mud is present, or Z_b if no fluid mud is present. Subscript \cdot_s , \cdot_m and \cdot_b refer to water surface, water – fluid mud interface and bed, respectively. Further, ν = kinematic viscosity and the eddy viscosity ν_T follows from the standard turbulence model within DELFT3D (for instance the k - ϵ model), which is not treated here.

The mass balance for suspended sediment reads:

$$\frac{\partial c}{\partial t} + \frac{\partial (u_i - \delta_{i3} W_s) c}{\partial x_i} - \frac{\partial}{\partial x_i} \left((D + \Gamma_T) \frac{\partial c}{\partial x_i} \right) = -D_m|_{z=Z_b} + E_m|_{z=Z_b} \quad (3.3)$$

Where δ_{ij} is the Kronecker delta, D = sediment diffusion coefficient and Γ_T is the eddy diffusivity.

For the mass balance for salt the standard formulation in DELFT3D is used. The equation of state accounts for effects of salinity (and temperature) only, **not** for the effects of suspended sediment, i.e. $\rho = \rho(S, T)$.

The fluid mud is assumed to appear in patches, as sketched in Fig. 1 and 2, which can move freely when tractive forces are large enough, both along and perpendicular to the coast (N.B. this implies no wave-setup for the time being). The behavior of the **lower, fluid mud layer** is governed by the momentum equation and the mass balance for sediment in the lower layer; the latter simplifies to an equation for the layer depth, as the sediment concentration in the fluid mud layer (bulk density) is assumed to be constant:

$$\frac{\partial \delta}{\partial t} + \frac{\partial u_{m,i} \delta}{\partial x_i} = (D_m - E_m + E_b - W_c) / c_m \quad (3.4)$$

The momentum equation reads:

$$\begin{aligned} \frac{\partial u_{m,i}}{\partial t} + u_{m,j} \frac{\partial u_{m,i}}{\partial x_j} - e_{ijk} f_k u_{m,j} + g \frac{\partial Z_s}{\partial x_i} + \frac{g \Delta \rho}{\rho_m} \left(\frac{\partial Z_m}{\partial x_i} - \frac{\partial Z_s}{\partial x_i} \right) - \nu_m \frac{\partial^2 u_{m,i}}{\partial x_j^2} + \\ - \frac{\tau_{Z_m,i}}{\rho_m \delta_m} + \frac{\tau_{Z_b,i}}{\rho_m \delta_m} = 0 \end{aligned} \quad (3.5)$$

The bed shear stress is given by a Bingham-kind rheological model:

$$\tau_{Z_b,i} = \left[\tau_B + \frac{\lambda}{8} \rho_m u_{m,j}^2 \right] \frac{b_{rel} u_{m,i}}{1 + b_{rel} \sqrt{u_{m,j}^2}} \quad (3.6)$$

A pure Bingham model cannot be applied, as the Bingham stress would induce an erroneous tractive force on the mud at small flow velocities. Therefore, we have added the relaxation b_{rel} , which has a value of about $10^5 - 10^6$ s/m to obtain finite values of τ_{Z_b} in the rang of $0 < u_m < u_{m,rel}$ m/s. For instance, for $b_{rel} = 10^5$ s/m, τ_{Z_b} varies linearly from $\tau_{Z_b,eff} = 0$ for $u_{m,rel} = 0$ to $\tau_{Z_b,eff} = 0.99 \tau_{Z_b}$ at $u_{m,rel} = 1$ mm/s. The stresses at the water-mud interface read:

$$\tau_{Z_m,i} = \frac{\lambda}{8} \rho u_j^2 \frac{u_i}{\sqrt{u_j^2}} \quad (3.7)$$

The shallow water equations discretized in the 2L FLUID MUD MODEL are solved with the finite difference Alternating Direction Implicit (ADI-)method (Stelling et al., 1986) on the staggered grid, sketched below. This staggering implies that the layer thickness at the

velocity points has to be obtained by averaging depth and water level values from neighboring points. This procedure was selected, as it allows for internal super-critical flow. The thickness of the water layer h^u for the velocity point $u_{i+1/2,j}$ for instance is presented in equ. (3.8) as an example.

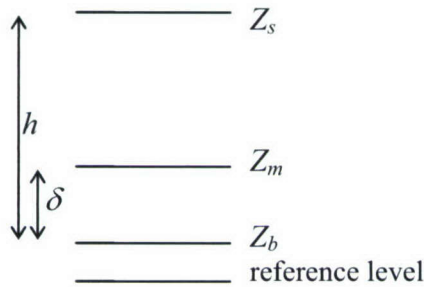
$$h_{i+1/2}^u = \frac{Z_{S_{i,j}} + Z_{S_{i+1,j}}}{2} - \frac{Z_{b_{i+1/2,j-1/2}} + Z_{b_{i+1/2,j+1/2}}}{2} \quad (3.8)$$

The flooding and drying procedure implies that the flow velocity is set to zero when $h_{i+1/2}^u < \varepsilon_h$, where ε_h is a user-defined threshold value. Such an inactive velocity grid point becomes active again when $h_{i+1/2}^u > 2\varepsilon_h$.

A net flow into a computational box not necessarily implies positive water depth in the box centre. Therefore an additional requirement has to be met: $h_{i,j}^\zeta > 0$, where superscript ζ refers to the water level point. The depth at a water level point is given by:

$$Z_{b_{i,j}}^\zeta = \max\left(Z_{b_{i+1/2,j+1/2}}, Z_{b_{i+1/2,j-1/2}}, Z_{b_{i-1/2,j+1/2}}, Z_{b_{i-1/2,j-1/2}}\right) \quad (3.9)$$

If this would result in a non-positive water volume in an active computational box, the procedure at this half-time step is repeated, but now with the computational box set dry. The flow velocity is set to zero in the four surrounding velocity points.



Definition of levels - see also Fig. 3

- = u -velocity component
- | = v -velocity component
- o = elevation of consolidated bed Z_b
- + = water or fluid mud elevation Z_s, Z_m

The upwind scheme for super-critical mud flow implies that the mud thickness is defined as a function of the mud flow direction. If $u_{i+1/2,j} > 0$ (to the right in the sketch above), the thickness of the fluid mud at this velocity point becomes $\delta_{i+1/2,j}^u = Z_{m_{i,j}} - Z_{b_{i,j}}^\zeta$, whereas for $u_{i+1/2,j} < 0$: $\delta_{i+1/2,j}^u = Z_{m_{i+1,j}} - Z_{b_{i+1,j}}^\zeta$. At dry points the thickness of the fluid mud layer is defined as a function of its slope, i.e. $\delta_{i+1/2,j}^u = Z_{m_{i,j}} - Z_{b_{i,j}}^\zeta$ for $Z_{m_{i,j}} > Z_{m_{i+1,j}}$ and $\delta_{i+1/2,j}^u = Z_{m_{i+1,j}} - Z_{b_{i+1,j}}^\zeta$ for $Z_{m_{i,j}} < Z_{m_{i+1,j}}$. Note that mass is always conserved with this procedure.

For the time integration the ADI-scheme is applied. For the one-dimensional case, the continuity equation becomes:

$$\frac{\delta_{i,j}^{l+1/2} - \delta_{i,j}^l}{\Delta t} + \frac{\delta_{i+1/2,j}^l u_{i+1/2,j} - \delta_{i-1/2,j}^l u_{i-1/2,j}}{\Delta x} = 0 \quad (3.10)$$

It can be shown (Stelling et al., 1998) that, for the upwind approach, positive definite water levels are guaranteed if the Courant condition for velocity is met:

$$\frac{\Delta t u_{i+1/2,j}}{\Delta x} < 1 \quad (3.11)$$

3.2 Modeling water-bed exchange processes

The exchange of sediment at the interface between the consolidated bed and the dilute suspension is modeled as follows:

Deposition from dilute suspension:

$$D_m|_{z=Z_b} = W_s c_{z=Z_b} \quad (3.12)$$

Where W_s [m/s] = settling velocity of the mud flocs in the dilute suspension and $c_{z=Z_b}$ [kg/m³] is the suspended sediment concentration close to the bed.

Erosion by dilute suspension:

$$E_m|_{z=Z_b} = M_E (\tau_b - \tau_{c,e}) \quad \text{for } \tau_b > \tau_{c,e} \quad (3.13)$$

where τ_b = bed shear stress, induced by currents and waves. The erosion parameter M_E [kg/m²/s/Pa] and the critical shear stress for erosion $\tau_{c,e}$ [Pa] follow either from user input, or are established through the formula by Van Kesteren (Winterwerp and Van Kesteren, 2004):

$$M_E = k_1 \frac{c_v \phi_{s,0} \rho_{dry}}{10 D_{50}} \quad \text{and} \quad \tau_{c,e} = 0.163 k_2 (PI)^{0.84} \quad (3.14)$$

Where c_v [m²/s] = the consolidation coefficient, $\phi_{s,0}$ [-] = initial (i.e. before swelling) volumetric concentration of the solids in the bed (solid fraction), ρ_{dry} [kg/m³] = dry density in the bed, D_{50} [m] = median size of primary floc size in the bed, PI [%] = plasticity index, and k_1 and k_2 are tuning coefficients, if necessary.

The exchange of sediment at the interface between the fluid mud layer and the consolidated bed and the dilute suspension is modeled as follows:

Deposition on fluid mud:

$$D_m|_{z=Z_m} = W_s c_{z=Z_m} \quad (3.15)$$

Where W_s [m/s] = settling velocity of the mud flocs in the dilute suspension and $c_{z=Z_m}$ [kg/m³] is the suspended sediment concentration in the dilute suspension close to the fluid mud layer.

Consolidation of fluid mud:

The consolidation rate is derived from Winterwerp and Van Kesteren (2004), where it is shown that the vertical velocity w_s of mud flocs in a consolidating bed with respect to a Eulerian reference frame is described by:

$$w_s = k \frac{\rho_s - \rho_w}{\rho_w} \phi + \frac{k}{g \rho_w} \frac{\partial \sigma_{zz}^{sk}}{\partial z} \quad (3.16)$$

Where ϕ [-] = solid fraction (= c_m/ρ_s , with c [kg/m³] = mass concentration), k [m/s] = permeability and σ_{zz}^{sk} [Pa] = the effective or skeleton stress. We apply fractal theory to establish k and σ_{zz}^{sk} :

$$k = K_k (\phi)^{-\frac{2}{3-n_f}} \quad \text{and} \quad \sigma_{zz}^{sk} = K_p (\phi)^{\frac{2}{3-n_f}} ; \quad \phi = c/\rho_s \quad (3.17)$$

Where n_f is the fractal dimension, and K_k and K_p are coefficients to be determined from consolidation experiments. Substitution into (3.16) and averaging over the fluid mud thickness δ yields (assuming that ϕ does not, or only slowly varies with time and depth):

$$V_c = \frac{c_m}{\delta} \int_{\delta} v_s dz = K_k \frac{\rho_s - \rho_w}{\rho_w} c_m (\phi)^{\frac{1-n_f}{3-n_f}} + \frac{K_k K_p}{\delta g \rho_w} c_m \quad (3.18)$$

Typical values for the various parameters amount to: $n_f = 2.5 - 2.7$, $K_k = 10^{-11} - 10^{-14}$ m/s and $K_p = 10^7 - 10^{10}$ Pa. This implies that for $c = 100 - 300$ kg/m³, V_c/c_m amounts to $10^{-8} - 10^{-10}$ m/s, hence the rate of consolidation can be neglected in applying the 2L FLUID MUD MODEL for the cases treated in this report. This agrees with our assumptions that the fluid mud behaves as an undrained fluid.

Erosion by fluid mud:

The same formula applied for the dilute suspension, i.e. equ. (3.13) can be applied for the erosion of the consolidated bed by the fluid mud layer as well. We note that the flow velocities of the fluid mud layer for the cases considered in this report are so low in general (often within the laminar flow regime), that the erosion of the sub-soil may be negligible in most cases.

Entrainment of fluid mud:

As mentioned above, the flow velocity of the fluid mud layer is very small in general, often within the laminar flow regime. Erosion of the fluid mud layer therefore takes place through entrainment by the turbulent water movements over the fluid mud layer, and the rate of entrainment reads (Winterwerp and Van Kesteren, 2004):

$$E_m = u_* \sqrt{\frac{0.5}{5.6 + Ri_*}} c_m \quad (3.19)$$

Where u_* [m/s] is the relevant shear velocity and Ri_* the bulk Richardson number defined as:

$$Ri_* = \frac{(\rho_m - \rho_w)gh}{\rho_w u_*^2} \quad (3.20)$$

The shear velocity u_* has a flow-induced component and a wave-induced component, as a turbulent wave-induced boundary layer may develop at the interface:

$$u_*^2 = u_{*,f}^2 + u_{*,w}^2 \quad (3.21)$$

$$u_{*,f}^2 = f_r U_1^2 \quad (3.22)$$

where f_r = friction coefficient ($f_r \approx 4 \cdot 10^{-4}$), U_1 = depth-averaged flow velocity in upper layer (e.g. Delft Hydraulics, 1974), and for the wave-induced friction we follow Soulsby and Clarke (2005):

$$u_{*,w}^2 = \frac{f_{ws}}{2} U_{orb,l}^2 \quad \text{with} \quad f_{ws} = 0.0521 Re^{-0.187}, \quad Re = \frac{U_{orb,l} A}{\nu} \quad (3.23)$$

Where $U_{orb,l}$ = amplitude wave orbital motion and A = wave semi-orbital excursion.

3.3 Mud-induced wave-damping

The two-layer fluid mud model by Gade (1958) is modified a bit and implemented in the SWAN-wave model. The SWAN-model is a two-dimensional fully spectral state-of-the-art wave propagation model developed by Delft University of Technology (Booij et al., 1999; Zijlema and Van der Westhuijsen, 2005). SWAN solves the balance equation for wave action density $N'(\sigma, \theta)$ [m²] per frequency σ ($= 2\pi/T$) and direction θ , which reads:

$\frac{DN'}{Dt} = \frac{DE'}{\sigma Dt} = \frac{S'}{\sigma} - \frac{S'_b}{\sigma} - \frac{S'_{b,m}}{\sigma} + \frac{S'_{nl}}{\sigma}$	(3.24)
---	--------

The wave action density N' is defined as $N' = E'/\sigma$, where $E'(\sigma, \theta)$ [m^2s] is the wave energy density and the total wave energy is obtained by integration over frequency and direction:

$$E = \int_0^{2\pi} \int_0^\infty E' d\sigma d\theta \quad (3.25)$$

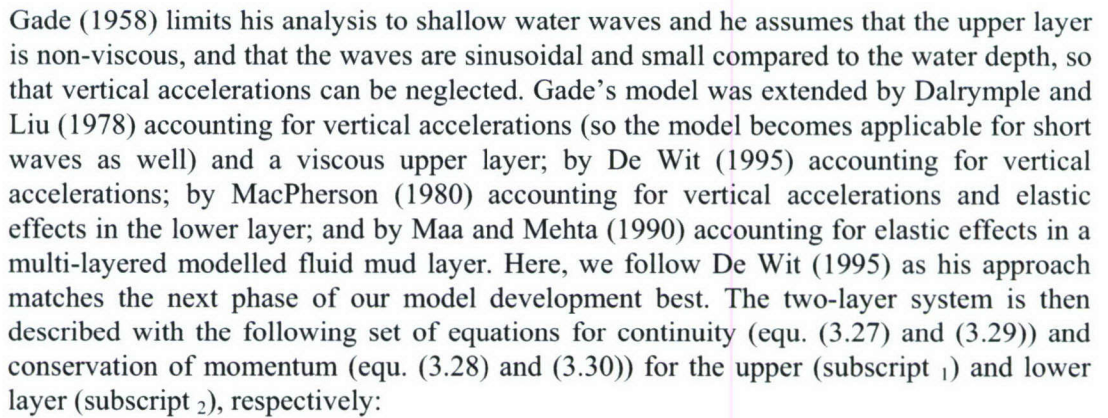
The root-mean-square of the orbital velocity at the seabed u_{orb} and the standard deviation of the water elevation $\hat{\eta}$ read:

$$u_{orb}^2 = \int_0^{2\pi} \int_0^\infty \frac{\sigma^2}{\sinh^2\{kh\}} \frac{E'}{g\rho} d\sigma d\theta \quad \text{and} \quad \frac{1}{2} \hat{\eta}^2 = \frac{E}{g\rho} \quad (3.26)$$

and the significant wave height $H_{1/3}$ follows from $E = \rho g H_{m0}^2 / 8$ [J/m^2], as the first moment and significant wave height are almost identical: $H_{1/3} \approx H_{m0}$. Note that within SWAN the energy is divided by ρg to yielding the energy density E [m^2], which leads to the other units given in these sections. In (3.24), $S'(\sigma, \theta)$ is a source term per wave frequency σ and direction θ accounting for wind input, $S'_b(\sigma, \theta)$ is a sink term accounting for energy dissipation by bed friction, white capping and depth-induced wave braking, $S'_{b,m}(\sigma, \theta)$ (with dimension [m^2] in SWAN) is a sink term accounting for viscous dissipation in the mud layer and $S'_{nl}(\sigma, \theta)$ accounts for non-linear wave-wave interactions. The first two and fourth terms have been implemented in the standard version of SWAN and are not elaborated here. The third term is modelled further to the two-layer approach by Gade (1958), where we assume that Gade's approach is applicable per wave direction, and that the individual solutions per wave direction may be added linearly. We note that the 2nd term (losses by friction) becomes much smaller when mud-induced damping is relevant, as the lower layer is now fluid (liquefied mud).

The material derivative D/Dt in equ. (3.24) contains advection of energy in geographical x - y space (i.e. the sum of the group velocity C_g and (depth) mean flow velocity U), and the propagation velocity in spectral σ - θ space. If we assume that $U \ll C_g$, only advection by the group velocity remains.

Fig. 3.2 shows the lay-out of the two-layer system and the various definitions; the fluid mud layer depicts a bounded internal wave. Free internal wave(s) in the fluid mud layer are irrelevant for the current problem, as these are far too long, and are therefore not treated here. It is important to note that this implies that the frequency σ and (complex) wave number k ($= k_r + ik_i$) are identical for the upper water layer and lower fluid mud layer.



$\frac{\partial u_2}{\partial t} + \frac{1}{\rho_m} \frac{\partial p_2}{\partial x} = v_m \frac{\partial^2 u_2}{\partial z^2}$	(3.30)
$\frac{\partial w_2}{\partial t} + \frac{1}{\rho_m} \frac{\partial p_2}{\partial x} = -g$	

in which p_1 and p_2 are the pressure in the upper and lower layer, u_1 and u_2 are the horizontal flow velocity in the upper and lower layer, w_1 and w_2 are the vertical flow velocity in the upper and lower layer with thickness h and δ_m , respectively, and v_m is the (constant) fluid

mud viscosity. The horizontal and vertical co-ordinate are given by x and z (note that x is in the direction θ of the waves), and t is time.

This set of equations is solved with the following boundary conditions:

- at free surface ($z = h + \delta_m$): $p = 0$, $\left(\eta_1 = \hat{\eta}_1 \exp\{i(kx - \sigma t)\}\right)$ and $w_1 = \partial \eta_1 / \partial t$,
- at interface ($z = \delta_m$): $\partial p / \partial z = 0$, $\partial u_2 / \partial z = 0$ and $w_1 = w_2 = \partial \eta_2 / \partial t$, and
- at consolidated bed ($z = 0$): $u_2 = w_2 = 0$.

where σ is the (real) wave frequency and k the complex wave number. Gade solved these equations with the harmonic method, yielding complex wave number and amplitudes of layer thickness and velocity (see also De Wit, 1995). Gade presented results for a uni-directional, mono-chromatic wave field. However, in SWAN a formulation for the energy dissipation $S'_{b,m}(\sigma, \theta)$ is required. The energy dissipation was obtained by Gade by integrating the work done by the surface waves over the wave period. As said, the relevant wave height was obtained from the harmonic solution of the set of equations (3.27) to (3.30). Gade (1958) obtained the dissipation per unit area and unit time, averaged over a wave cycle from the mean work (W) done by the surface waves on the internal waves per unit area:

$$W = -\frac{1}{T} \int_0^T p \frac{dn}{dt} dt \approx -\frac{1}{T} \int_0^T p \frac{d\delta_m}{dt} dt \quad (3.3^*)$$

Where p = the pressure and n = the normal vector to the interface, which is correct for $\zeta_m \ll \lambda_m$. Extending Gade's analysis¹⁾, assuming that superposition of the solutions is allowed, the energy dissipation per wave frequency σ and direction θ reads:

$$S'_{b,m}(\theta, \sigma) = \alpha g h_0 \sigma R \frac{\hat{\eta}_2}{\hat{\eta}_1} \sin\{\phi' - \phi\} E' \quad (3.31)$$

The complex wave number ($k = k_r + ik_i$) follows from De Wit (1995):

$$\left[\frac{\rho_m - \rho_0}{\rho_m} \frac{gk}{\sigma^2} \left(k\delta_{m,0} - \frac{k}{\lambda_g} \tanh\{\lambda_g \delta_{m,0}\} \right) - 1 \right] \left[\frac{gk}{\sigma^2} \tanh\{kh_0\} - 1 \right] + \left[-\frac{\rho_0}{\rho_m} \left(k\delta_{m,0} - \frac{k}{\lambda_g} \tanh\{\lambda_g \delta_{m,0}\} \right) \right] \left[\frac{gk}{\sigma^2} - \tanh\{kh_0\} \right] = 0 \quad (3.32)$$

where $\lambda_g = (1-i)\sqrt{\sigma/2\nu_m}$, from which k_r , k_i and their modulus $R = (k_r^2 + k_i^2)/\sigma^2$ and argument (phase angle between water elevation and flow velocity) $\phi = 2\arctan\{k_i/k_r\}$ can be computed (i.e. $(k/\sigma)^2 = R \exp\{i\phi\}$). De Wit (1995) showed that (3.32) agrees with Gade's dispersion relation for shallow water waves. For one-layer

¹⁾ Note that Gade's paper contains a (typing)error in the elaboration of the energy losses: equ. (3.31) should contain a σ .

flow (water only), $\rho_m = \rho_0$ and $\delta_{m,0} = 0$, and equ. (3.32) reduces to the classical dispersion relation $\sigma^2 = gk \tanh kh_0$.

The relation between the surface and internal waves follows from the ratio of their (complex) amplitudes, which can be found from the ratio $(w_2(z = Z_m)/w_1(z = Z_s))$ of the vertical velocity at the water surface and interface, as only bounded internal waves are considered. This ratio can be obtained from De Wit (1995) and yields:

$$\frac{w_2}{w_1} = \frac{\hat{\eta}_2}{\hat{\eta}_1} e^{i\phi'} = S e^{i\phi'} = \frac{\sigma^2 \left(1 + (\sinh \{kh_0\})^2\right) - gk \sinh \{kh_0\} \cosh \{kh_0\}}{\sigma^2 \cosh \{kh_0\}} \quad (3.34)$$

Expanding (3.34) around $kh_0 = 0$ with a Taylor series gives:

$$\frac{\hat{\eta}_2}{\hat{\eta}_1} e^{i\phi'} = 1 - \frac{gk}{\sigma^2} kh_0 + \frac{1}{2} (kh_0)^2 - \frac{gk}{6\sigma^2} (kh_0)^3 + \frac{1}{24} (kh_0)^4 + O\{(kh_0)^5\} + \dots \quad (3.35)$$

which for shallow water ($kh_0 \ll 1$) degenerates to:

$$\frac{w_2}{w_1} = \frac{\hat{\eta}_2}{\hat{\eta}_1} e^{i\phi'} = 1 - \frac{gk}{\sigma^2} kh_0 = 1 - gh_0 \left(\frac{k}{\sigma}\right)^2 = 1 - gh_0 Re^{i\phi} \quad \text{for } kh_0 \ll 1 \quad (3.36)$$

The modulus S and argument ϕ' from equ. (3.34) have been obtained with MAPLE and read²⁾:

$$\sigma^4 S^2 = \left(gk_r \sin h_0 k_i \cosh h_0 k_r + gk_i \cos h_0 k_i \sinh h_0 k_r - \sigma^2 \sin h_0 k_i \sinh h_0 k_r \right)^2 + \left(gk_r \cos h_0 k_i \sinh h_0 k_r - gk_i \sin h_0 k_i \cosh h_0 k_r - \sigma^2 \cos h_0 k_i \cosh h_0 k_r \right)^2 \quad (3.37)$$

$$\tan \phi' = \frac{\left(gk_r \cos h_0 k_i \sinh h_0 k_r - gk_i \sin h_0 k_i \cosh h_0 k_r - \sigma^2 \cos h_0 k_i \cosh h_0 k_r \right)}{\left(gk_r \sin h_0 k_i \cosh h_0 k_r + gk_i \cos h_0 k_i \sinh h_0 k_r - \sigma^2 \sin h_0 k_i \sinh h_0 k_r \right)} \quad (3.38)$$

Hence, as $\phi < |\phi'|$ and $\phi' < 0$ is always true, $S'_{b,m} > 0$ (e.g. Gade, 1958).

It is noted that our analyses show some inconsistencies in the dispersion relation and the other relations, which may be the result of an error in the dispersion relation. This is being checked at this moment. The dispersion relation may therefore have to be altered in the near future.

²⁾ Note that Gade's relations for S and ϕ' read: $R = (k_r^2 + k_i^2) / \sigma^2$ and $\phi' = 2 \tan \{k_i / k_r\}$.

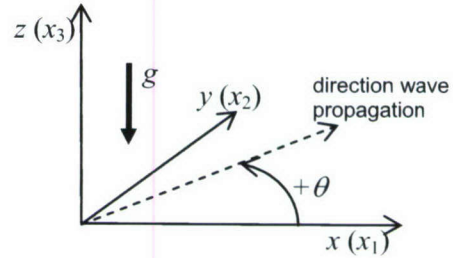
The mud properties $\delta_m(x,y)$, ρ_m and ν_m follow from measurements or the models presented further in this paper. Finally, we have added an extra calibration coefficient α in (3.31) to account for possible non-linear effects allowing a better tuning of SWAN to the observations, if necessary.

Gade (1958) and Dalrymple and Liu (1978) found that maximum wave attenuation occurs when the thickness of the fluid mud layer amounts to about 1.3 times its boundary layer thickness $\Delta_m (= \sqrt{\sigma/2\nu_m})$, which agrees well with Gade's laboratory observations (see also Section 5).

3.4 Wave-induced mud transport

In this section a model for wave-induced mud transport is derived. It can be shown that the tractive force by wave-induced interfacial drag is small compared to the forces by the radiation stress. Only the effects of radiation stress are therefore accounted for.

Here we apply a right-handed co-ordinate system with positive z -axis (x_3 -axis) positive upward. Waves travel at an angle θ with the positive x -axis. Note that x_I is not necessarily perpendicular to the coast.



Longuet-Higgins (1953, 1958) has shown through a simple momentum balance that momentum losses by bed friction in the wave boundary layer are compensated by a tractive force, which has the form of the well-known Reynolds stresses. These stresses are commonly referred to as radiation stresses and the tractive forces are known as streaming.

It can be shown (see equ. (3.41)) that the radiation stress (i.e. the wave momentum fluxes) is proportional to the wave energy in the wave boundary layer. Therefore, any change in the wave energy, for instance due to shoaling, bed friction, viscous damping, etc., must induce a change in radiation stress, hence tractive forces. In cross-shore direction this accounts for the well-known wave set-up, and in long-shore direction in the well-known long-shore wave-induced currents, which can be quite large, in particular in the surf zone.

First, the more general case is treated. The hydrostatic momentum equation is averaged over the wave period (e.g. Phillips, 1977)

$$\frac{\partial u_\alpha}{\partial t} + u_j \frac{\partial u_\alpha}{\partial x_j} - e_{\alpha\beta k} f_k u_\alpha + \frac{1}{\rho} \frac{\partial p}{\partial x_\alpha} - \frac{1}{\rho} \frac{\partial \tau_{j\alpha}}{\partial x_j} = F_\alpha = -\frac{1}{\rho} \frac{\partial S_{\alpha\beta}}{\partial x_\beta} \quad (3.35)$$

Thus for instance in x -direction:

$$\frac{\partial u}{\partial t} + u \frac{\partial u}{\partial x} + v \frac{\partial u}{\partial y} + w \frac{\partial u}{\partial z} + \dots = -\frac{1}{\rho} \left(\frac{\partial S_{xx}}{\partial x} + \frac{\partial S_{xy}}{\partial y} \right) \quad (3.36)$$

The wave-induced tractive force F_α is determined by the gradients in the so-called radiation stress $S_{\alpha\beta}$. Here α and β ($= 1, 2$) correspond to the horizontal co-ordinates x and y only, whereas j ($= 1, 2, 3$) corresponds to the co-ordinates x, y, z . The radiation stress tensor $S_{\alpha\beta}$ is given by (e.g. Mei, 1989; Dingemans, 1997):

$$S_{\alpha\beta} = \begin{bmatrix} S_{xx} & S_{xy} \\ S_{yx} & S_{yy} \end{bmatrix} = \begin{bmatrix} (n \cos^2 \theta + n - 1/2)E & (n \cos \theta \sin \theta)E \\ (n \cos \theta \sin \theta)E & (n \sin^2 \theta + n - 1/2)E \end{bmatrix} \quad (3.37)$$

where $n = C_g/c = k_r/\sigma \cdot d\sigma/dk_r$, C_g = group velocity, c = wave celerity. In case of clear water, we find the common relation $n = C_g/c = 1/2 + k_r h / \sinh\{2k_r h\}$, from which, by differentiating the normal xx -component to x , we find for instance:

$$\begin{aligned} \frac{\partial S_{xx}}{\partial x} &= \frac{\partial}{\partial x} (n \cos^2 \theta + n - 1/2)E = \frac{\cos \theta}{c} \frac{\partial}{\partial x} (EC_g \cos \theta) + \frac{\partial}{\partial x} \left(\frac{k_r h E}{\tanh\{2k_r h\}} \right) = \\ &= \frac{\partial}{\partial x} \left(\frac{k_r h E}{\tanh\{2k_r h\}} \right) + \frac{\cos \theta}{c} \frac{\partial P_x}{\partial x} = \frac{\partial}{\partial x} \left(\frac{k_r h E}{\tanh\{2k_r h\}} \right) - \frac{\cos \theta}{c} D \end{aligned} \quad (3.38)$$

as $\partial P_x / \partial x + D = 0$, where D = total dissipation rate per unit area. Hence, we find for the gradient of the radiation stress tensor:

$$\frac{\partial S_{\alpha\beta}}{\partial x_\beta} = \begin{bmatrix} \frac{\partial}{\partial x} \left\{ \frac{k_r h E}{\sinh\{2k_r h\}} \right\} - \frac{D \cos \theta}{c} & -\frac{D \cos \theta}{c} \\ -\frac{D \sin \theta}{c} & \frac{\partial}{\partial y} \left\{ \frac{k_r h E}{\sinh\{2k_r h\}} \right\} - \frac{D \sin \theta}{c} \end{bmatrix} \quad (3.39)$$

where c = phase speed (celerity), k_r = wave number, h = water depth, E = wave energy density ($E = \frac{1}{2} \rho g \hat{\eta}^2 \approx \frac{1}{8} \rho g H_{1/3}^2$), $\hat{\eta}$ = wave amplitude, $H_{1/3}$ = significant wave height, and θ = angle between wave propagation and x_I -axis.

The gradients in the normal component of the radiation stress generate a wave-induced set-up (set-down) of the mean water level, whereas the shear component of the radiation stress generates a tractive force. These terms should be added to the momentum equation of the lower layer (3.5). Furthermore, wave set-up due to wave dissipation in the upper layer induces an additional slope (4th term of (3.5)) – this effect however is already accounted for in DELFT3D. To enable the modeling of the effects of the radiation stresses on the momentum balance within the DELFT3D-concept, we apply the so-called GLM-approach, as discussed by for instance Groeneweg (1999) and Walstra et al. (2000). This implies that the momentum equation is re-written in the well-known Eulerian way, but the velocities computed refer to the Generalized Lagrangian Mean reference frame, and have to be corrected for the Stokes' drift (see below).

Hence, the momentum equation for the lower layer then reads (compare with equ. (3.5)):

$$\begin{aligned} \frac{\partial u_m^L}{\partial t} + u_m^L \frac{\partial u_m^L}{\partial x} + v_m^L \frac{\partial u_m^L}{\partial y} + f v_m^L + g \frac{\partial Z_s}{\partial x} + \frac{g \Delta \rho}{\rho_m} \frac{\partial}{\partial x} (Z_m - Z_s) - v_m^L \frac{\partial^2 u_m^L}{\partial x^2} + \\ - \frac{\tau_{m,x}}{\rho_m \delta_m} - \frac{\tau_{m,Z_m,x}}{\rho_m \delta_m} \Big|_{z=Z_i} + \frac{\tau_{m,Z_b,x}}{\rho_m \delta_m} \Big|_{z=Z_b} = 0 \end{aligned} \quad (3.40a)$$

$$\begin{aligned} \frac{\partial v_m^L}{\partial t} + u_m^L \frac{\partial v_m^L}{\partial x} + v_m^L \frac{\partial v_m^L}{\partial y} - f u_m^L + g \frac{\partial Z_s}{\partial y} + \frac{g \Delta \rho}{\rho_m} \frac{\partial}{\partial y} (Z_m - Z_s) - v_m^L \frac{\partial^2 v_m^L}{\partial y^2} + \\ - \frac{\tau_{m,y}}{\rho_m \delta_m} - \frac{\tau_{m,Z_m,y}}{\rho_m \delta_m} \Big|_{z=Z_i} + \frac{\tau_{m,Z_b,y}}{\rho_m \delta_m} \Big|_{z=Z_b} = 0 \end{aligned} \quad (3.40b)$$

where superscript L refers to the GLM reference frame. Note that the force induced by the radiation stresses $\partial S_{\alpha\beta} / \partial x_\beta$ are computed within SWAN as the FORCE $\tau_{m,\alpha}$ (see below). It is further noted that the wave field in the real world generally comprises a spectrum. SWAN accounts for this spectrum by averaging wave number and wave period weighted for the energy at a specific frequency. This approach is applied here as well. The mean real and imaginary wave number \bar{k}_r and \bar{k}_i , mean wave frequency $\bar{\sigma}$, mean wave direction $\bar{\theta}$, mean wave celerity $\bar{c} \equiv \bar{c}_i = \bar{\sigma} / \bar{k}_r$ and mean value of the radiation stresses $\bar{S}_{\alpha\beta}$ are defined as follows:

$$\begin{aligned} \bar{\sigma} &= \frac{\int_0^{2\pi} \int_0^\infty \sigma(\theta) E'(\sigma, \theta) d\sigma d\theta}{\int_0^{2\pi} \int_0^\infty E'(\sigma, \theta) d\sigma d\theta} & [\text{s}^{-1}] & \text{TM01} \\ \bar{k}_r &= \frac{\int_0^{2\pi} \int_0^\infty k_r(\sigma, \theta) E'(\sigma, \theta) d\sigma d\theta}{\int_0^{2\pi} \int_0^\infty E'(\sigma, \theta) d\sigma d\theta} & [\text{m}^{-1}] & \text{WLENMR} \\ \bar{k}_i &= \frac{\int_0^{2\pi} \int_0^\infty k_i(\sigma, \theta) E'(\sigma, \theta) d\sigma d\theta}{\int_0^{2\pi} \int_0^\infty E'(\sigma, \theta) d\sigma d\theta} & [\text{m}^{-1}] & \text{WLENMI} \\ \bar{\theta} &= \arctan \left\{ \frac{\int_0^{2\pi} \int_0^\infty E'(\sigma, \theta) \sin \theta d\sigma d\theta}{\int_0^{2\pi} \int_0^\infty E'(\sigma, \theta) \cos \theta d\sigma d\theta} \right\} & [\text{rad}] & \text{DIR} \\ \bar{S}_{xx} &= \rho g \int_0^{2\pi} \int_0^\infty (n \cos^2 \theta + n - 1/2) E'(\sigma, \theta) d\sigma d\theta \\ \bar{S}_{xy} &= \bar{S}_{yx} = \rho g \int_0^{2\pi} \int_0^\infty (n \sin \theta \cos \theta) E'(\sigma, \theta) d\sigma d\theta \\ \bar{S}_{yy} &= \rho g \int_0^{2\pi} \int_0^\infty (n \sin^2 \theta + n - 1/2) E'(\sigma, \theta) d\sigma d\theta \\ & \left. \begin{aligned} \bar{S}_{xx} \\ \bar{S}_{xy} \\ \bar{S}_{yy} \end{aligned} \right\} & [\text{J/m}^2] & \text{computed in SWAN} \\ \tau_x &= -\frac{\partial \bar{S}_{xx}}{\partial x} - \frac{\partial \bar{S}_{xy}}{\partial y} \quad \text{and} \quad \tau_y = -\frac{\partial \bar{S}_{xy}}{\partial x} - \frac{\partial \bar{S}_{yy}}{\partial y} & [\text{Pa}] & \text{FORCE} \end{aligned} \quad (3.4^*)$$

Where $n(\sigma, \theta) = k_r(\sigma, \theta) / \sigma(\theta) \cdot d\sigma(\theta) / dk_r(\sigma, \theta)$. See Section 3.3 for definitions.

Note that the radiation stress $\bar{S}_{xx} = \rho_m g \int_0^{2\pi} \int_0^\infty (n \cos^2 \theta + n - 1/2) E'_m(\sigma, \theta) d\sigma d\theta$, etc. in the lower layer is not computed in SWAN and should be obtained from the ratio between the total wave energy in the fluid mud layer E_m (c.q. E'_m) and the total energy of the surface waves E (c.q. E'), using relation (3.34). The same holds for the tractive force:

$$E_m = \frac{\rho_m \hat{\eta}_2^2}{\rho_1 \hat{\eta}_1^2} E, \quad \text{hence} \quad \tau_{m,\alpha} = \frac{\rho_m \hat{\eta}_2^2}{\rho_1 \hat{\eta}_1^2} \tau_\alpha \quad (\text{FORCE}) \quad (3.42)$$

The actual Eulerian velocity of the fluid mud layer follows from:

$$u_{m,i} = u_{m,i}^E = u_{m,i}^L - U_{m,i}^S = u_{m,i}^L - \frac{E_m}{\rho_m \delta} \frac{\bar{k}_{r,i}}{\bar{\sigma}}; \quad \bar{k}_{r,x} = \bar{k}_r \cos \bar{\theta}, \quad \bar{k}_{r,y} = \bar{k}_r \sin \bar{\theta} \quad (3.43)$$

where superscript E and S refer to Eulerian reference frame and Stokes' drift, respectively.

The bed shear stress is related with the Bingham strength τ_B through a rheological model (e.g. Section 3.6):

$$\tau_{m,z_b,i} = \left[\tau_B + \frac{\lambda}{8} \rho_m (u_{m,j}^L)^2 \right] \frac{b_{rel} u_{m,i}^L}{1 + b_{rel} \sqrt{(u_{m,j}^L)^2}} \quad (3.44)$$

and the stresses at the water-mud interface, assuming $u_i \gg u_{i,m}^L$:

$$\tau_{m,z_i} = \frac{\lambda}{8} \rho u_j^2 \frac{u_i}{\sqrt{u_j^2}} \quad (3.45)$$

3.5 A criterion for liquefaction of the mud bed

In this section we propose a method to determine whether a mud bed liquefies and, if so, to compute the thickness and the extension of the liquefied mud layer. This method should include the liquefaction of the muddy seabed by waves and the strength recovering after the waves in calm weather conditions. Moreover, the effects of stress history should be accounted for. A model for strength recovery is proposed in Section 3.6.

At present, no complete theory exists. There is some theoretical work, based on the Biot model (Sumer and Fredsøe, 2002; McDougal, et al., 1989) and some experimental work (Alba et al., 1976) published, but none of the studies are complete and applicable to the 2L modeling proposed here. Therefore, we propose a new method, which is partly based on earlier work carried out at Delft Hydraulics (Van Kesteren and Cornelisse, 1995).

It is illustrative to discuss the stress/strength evolution in the bed first in a qualitative way. Consider a flat seabed of well-consolidated mud. The vertical skeleton (effective) stress at a certain depth is determined by the density and packing of the sediment and that depth. The

lateral skeleton stress follows from the coefficient of lateral stress (or coefficient of earth pressure at rest) K_0 :

$$\sigma_{1,2} = K_0 \sigma_3 \quad (3.42)$$

where $\sigma_3 (= \int_z \rho_{dry} g dz)$, with $\rho_{dry}(z)$ = dry density of sediment and z = depth into the soil) is the vertical principal skeleton stress and σ_1 and σ_2 are the two horizontal principal stress components. The coefficient of lateral stress K_0 is related to the angle of internal friction φ through:

$$K_0 = \frac{\nu}{1-\nu} \approx 1 - \sin(\varphi) \quad (3.43)$$

where ν is the Poisson ratio. The stress conditions in the soil can be visualized in a σ - τ diagram, the so-called Mohr diagram, as depicted in Fig. 3.3, showing two circles of Mohr at two different depths in the seabed, where σ = normal stress and τ is shear stress. For simplicity, we draw the circles in one plane only. Note that we depict the skeleton (effective) stresses. For water, $K_0 = 1$ and $\sigma_1 (= \sigma_2) = \sigma_3$ and the Mohr circles degenerate to one point on the σ -axis; in case σ represents skeleton stresses only, $\sigma_1 (= \sigma_2) = \sigma_3 = 0$, of course. In case of very fresh mud deposits, $K_0 = 0$, and $\sigma_1 (= \sigma_2) = 0$.

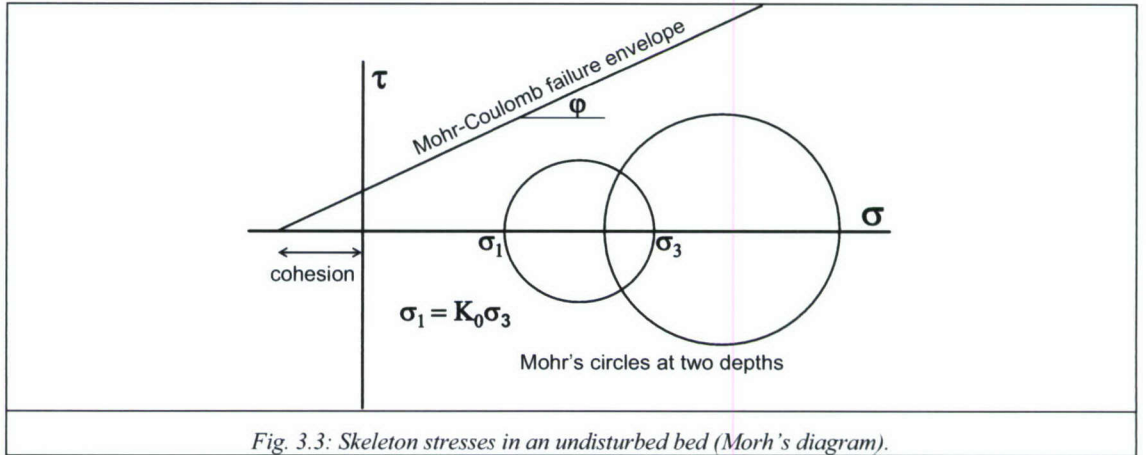


Fig. 3.3: Skeleton stresses in an undisturbed bed (Mohr's diagram).

Next, let us depict the stresses in the seabed induced by regular waves with wave height H_s and wave number k and wave frequency ω in x -direction. Then, the wave-induced water pressure (we can omit the effects of the wave-induced bed-shear stresses, which hardly generate stresses within the bed) on the seabed reads (Flamant – see Yamamoto et al., 1978; Sumer and Fredsøe, 2002):

$$P_w = \frac{\rho g H \cos(\omega t - kx - \psi)}{2 \cosh\{kh\}} \quad (3.44)$$

Where h the local water depth, and φ is phase angle. The amplitude of the stresses p_w in an elastic bed reads:

$$p_w = \frac{\rho g H}{2 \cosh\{kh\}} \frac{F}{F - \tanh\{kh\}} \quad \text{with} \quad F = \frac{G k^2}{\rho_w \omega^2 (1 - \nu)} \quad (3.45)$$

where G is the elastic shear modulus. For the time being we assume non-elastic bed properties ($G = F = \infty$), e.g. Sumer and Fredsøe (2002), so that the stress amplitude becomes $p_w = \rho g H / 2 \cosh\{kh\}$, and the total skeleton stresses within the bed read (where superscript ^w refers to wave-induced stresses):

$$\begin{aligned} \sigma_{zz} &= \sigma_{zz}^w + \int_z \rho_{dry} g dz' = p_w (1 + kz) e^{-kz} \cos(\omega t - \psi) + \int_z \rho_{dry} g dz' \\ \sigma_{xx} &= \sigma_{xx}^w + K_0 \int_z \rho_{dry} g dz' = p_w (1 - kz) e^{-kz} \cos(\omega t - \psi) + K_0 \int_z \rho_{dry} g dz' \\ \sigma_{xz} &= \sigma_{xz}^w = p_w k z e^{-kz} \sin(\omega t - \psi) \end{aligned} \quad (3.46)$$

We have also added the effect of the isotropic stresses at depth z by the own weight of the sediment, with $\rho_{dry}(z)$ = dry density of the sediment bed. Perpendicular to the waves in the horizontal plane (y -direction), the normal stress is found from:

$$\sigma_{yy} = \frac{\sigma_{xx}^w + \sigma_{zz}^w}{2} + K_0 \int_z \rho_{dry} g dz' = p_w e^{-kz} \cos(\omega t - \psi) + K_0 \int_z \rho_{dry} g dz' \quad (3.47)$$

If the wave-induced stresses are large enough, bonds between the flocs in the bed will be broken and the effective stress decreases and a water overpressure is building up. This is sketched in Fig. 3.4, showing that the original Mohr circle of Fig. 3.3 (dotted line) shifts to the left, as σ_3 and K_0 become smaller (hence σ_1 decreases more than σ_3). We note that the circle becomes larger as the shear stress increases, which is due to the fact that less bonds have to carry the same stress. When the mud lies on a slope, partial liquefaction may be sufficient to destabilize the bed (mud flow).

Because of the breakage of bonds, also the cohesion and angle of repose φ (and thus K_0 , e.g. equ. (3.43)) decrease, resulting in a translation and rotation of the Mohr-Coulomb failure envelope, as sketched in Fig. 3.4 by the dashed line. Note that we assume undrained conditions, which is generally true for the conditions at which the 2L fluid mud model is applicable (e.g. Winterwerp and Van Kesteren, 2004).

The wave-induced stresses, given in equ. (3.44) should be added as well to the stress diagram of Fig. 3.4. This is done for one arbitrary time, indicated by the solid circle in Fig. 3.4 - basically a family of circles is found, depending on the phase of the wave. When a critical number of bonds is broken, the mud bed fails and becomes fluid, and the circles of Mohr become smaller and smaller as the fluid mud is no longer able to sustain considerable shear stresses (we get a non-Newtonian fluid); the circles may even degenerate to a line on the σ -axis around the origin of the σ - τ diagram if the fluid cannot sustain any shear stresses.

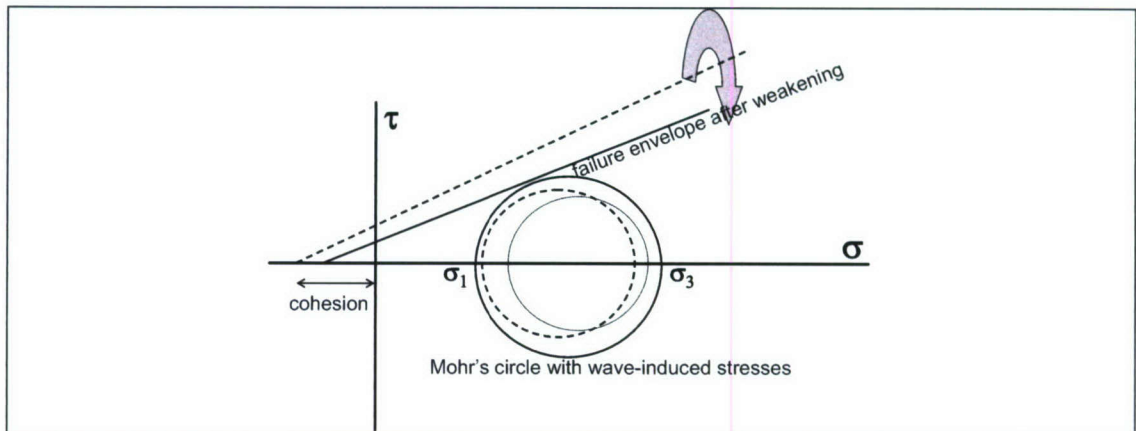


Fig. 3.4: Skeleton stresses induced by waves in a muddy seabed.

After passage of the waves, the mud can regain strength through a kind of consolidation during which the bonds between the flocs are restored, under quite conditions. This is depicted schematically in Fig. 3.5, showing that the stresses, angle of repose and cohesion are restored (e.g. Section 3.6).

As said, the liquefaction process was considered to take place under undrained conditions, so no water was expelled. However, in practice this may not be the case entirely, as a result of which the sediment's bulk density may increase a bit. This implies that when all bonds are restored again, the bed may become stronger than before the liquefaction process. This is quantified by the so-called Over Consolidation Ratio (OCR), which can be measured from oedometer tests (Lambe and Whitman, 1979).

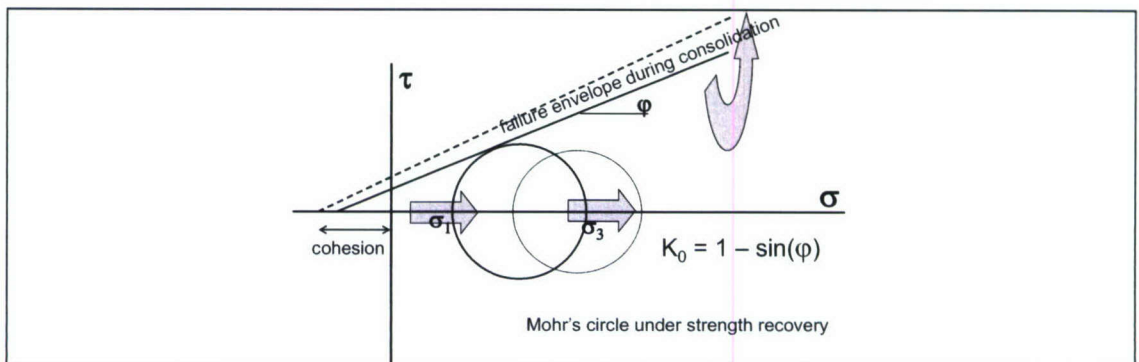


Fig. 3.5: Skeleton stresses under strength recovery – no wave action.

In theory, the description above can be used to quantify the liquefaction behavior or liquefaction potential of a seabed if we know how the skeleton stresses decrease with number of wave cycles. The latter can be achieved through cyclical roto-viscometer tests or cyclical triaxial tests. However, it is clear that the use of Mohr-circles is not very practical, as they have to be drawn for each depth in the seabed and for each phase in the wave cycle. Therefore, it is more common to visualize the stresses in the so-called p - q diagram, where p is the isotropic stress and q is the deviatoric stress. A cyclical load then yields the stress path depicted in Fig. 3.6, where the stresses follow typical butterfly paths. When the stresses exceed the failure envelope, liquefaction can be expected.

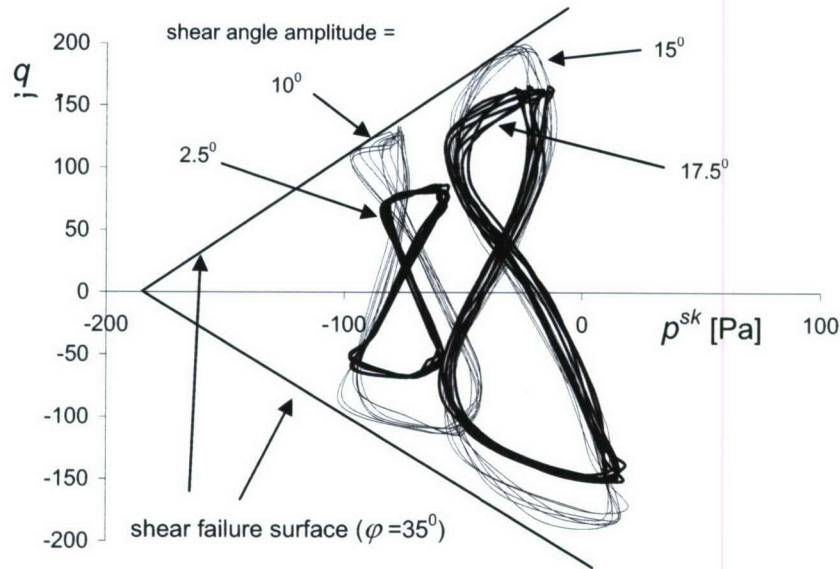


Fig. 3.6: Variation of shear stress and water pressure during cyclical shear tests on Haringvliet mud at various shear angle amplitudes (Van Kesteren and Cornelisse, 1995).

In our model we make use of the observation that with the breakage of bonds, the water overpressure rises with number of wave cycles. Full liquefaction is found after N_ℓ cycles, where N_ℓ can vary between a few 10 cycles to many thousands (and more), depending on the wave characteristics and the strength (history) of the bed, e.g. Sumer and Fredsøe (2002). The results of experiments on granular material (sand) by Alba et al. (1976) are depicted in Fig. 3.7 as an example, showing the so-called Cyclical Stress Ratio (CSR) $\hat{q}(z)/p_0(z)$, i.e. the ratio of the amplitude of the stress deviator in the seabed and the initial skeleton (effective) stress prior to liquefaction as a function of the number of wave cycles and initial packing.

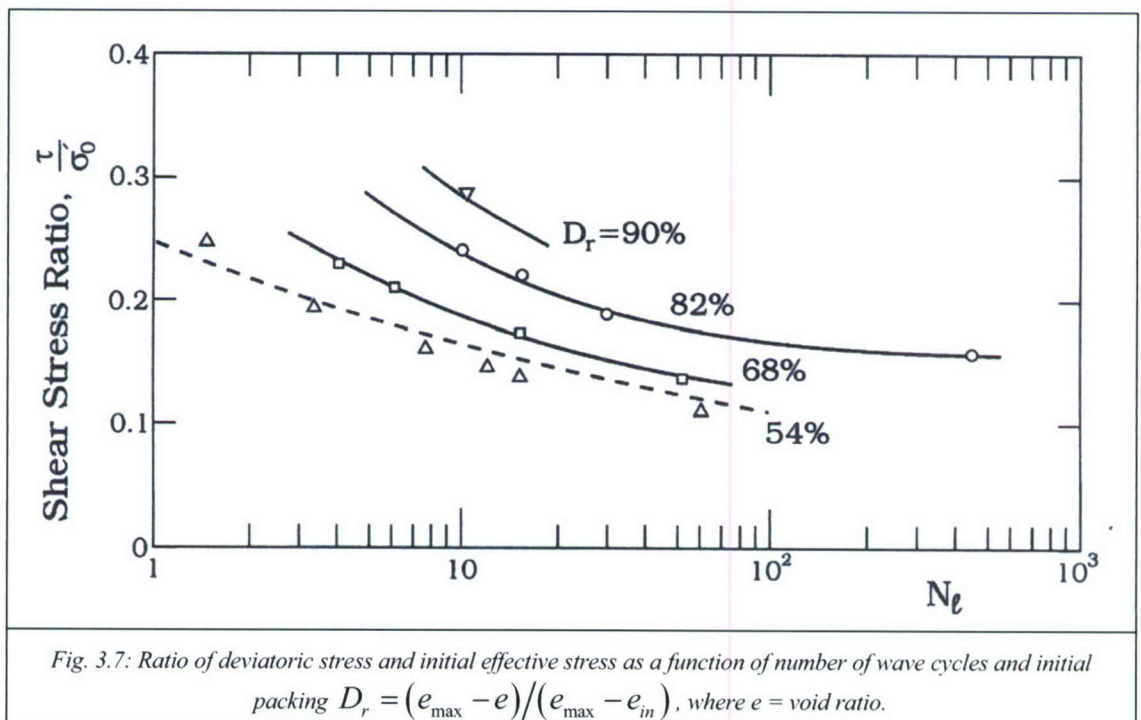


Fig. 3.7: Ratio of deviatoric stress and initial effective stress as a function of number of wave cycles and initial packing $D_r = (e_{\max} - e)/(e_{\max} - e_{in})$, where e = void ratio.

Van Kesteren (2000) carried out cyclical triaxial tests on sediments from the Orange River, the results of which are shown in Fig. 3.8. The results suggest a power law relation between the development of the deviatoric stresses and the number of wave cycles. Note that liquefaction of the well-consolidated clayey-silt sample is only observed after about 60,000 cycles. As the cycle period was set at 15 s, this would imply liquefaction after 10 days only. In contrast, the sandy sample liquefies after about 10 cycles, which is in agreement with the observations of Fig. 3.8.

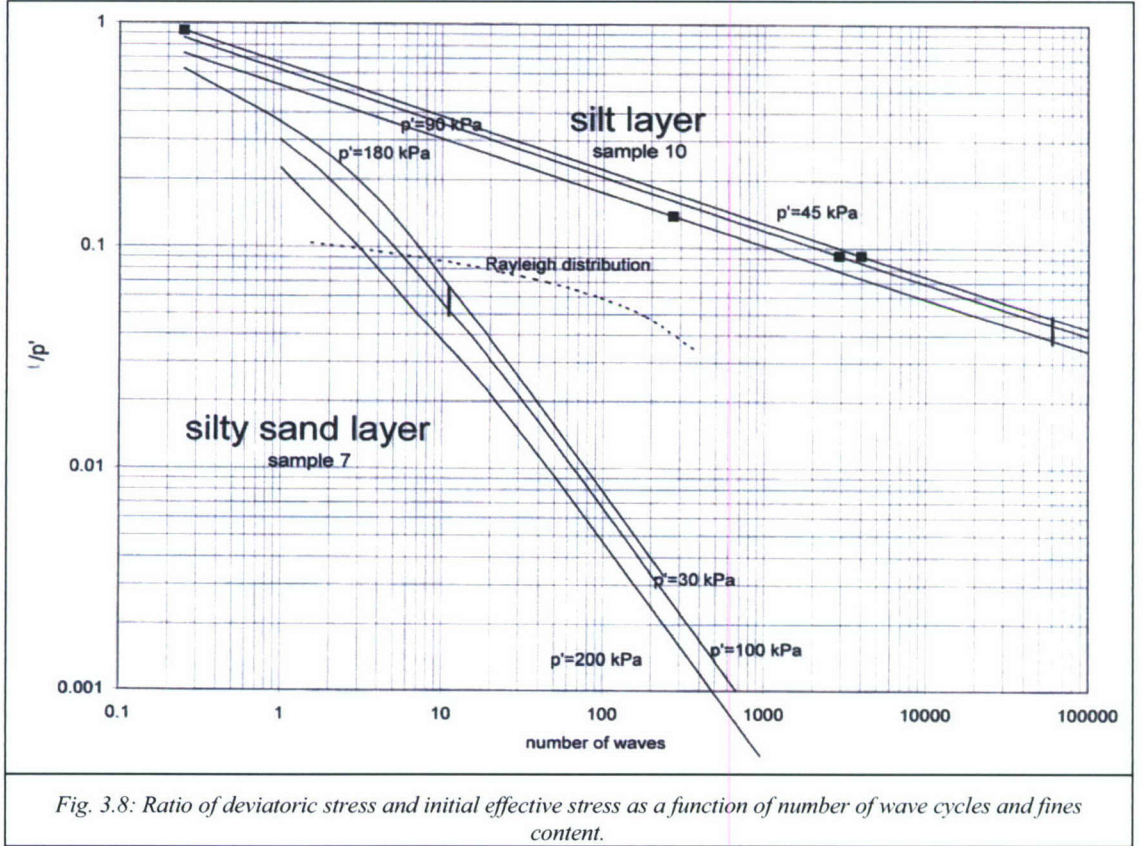


Fig. 3.8: Ratio of deviatoric stress and initial effective stress as a function of number of wave cycles and fines content.

These results suggest that we can establish the following criterion for failure of the bed, i.e. liquefaction occurs when:

$$\hat{q} \geq \hat{q}_{cr} = \lambda_s \alpha p_0 \left(\frac{N_\ell}{N} \right)^\beta \quad \text{or} \quad \frac{1}{\lambda_s \alpha} \frac{\hat{q}}{p_0} \left(\frac{N}{N_\ell} \right)^\beta \geq 1 \quad (3.48)$$

Where N is the number of actual wave cycles, N_ℓ is the number of cycles at which liquefaction occurs, and α and β have to be determined empirically from cyclical triaxial tests at a number of stress conditions. The clayey-silt sample of Fig. 10 would yield: $\alpha = 0.6$ and $\beta = -0.24$ (e.g. Van Kesteren, 2000). The structure parameter λ_s is discussed in Section 3.6; λ_s varies between 0 and 1.

The isotropic and deviatoric stress follow from (e.g. Winterwerp and van Kesteren, 2004):

$$\begin{aligned} p &= I_1/3 \\ q &= \sqrt{I_1^2 - 3I_2} \end{aligned} \quad (3.49)$$

In which the stress invariants I_i are defined as:

$$\begin{aligned} I_1 &= \sigma_{xx} + \sigma_{yy} + \sigma_{zz} \\ I_2 &= \sigma_{xx}\sigma_{yy} + \sigma_{yy}\sigma_{zz} + \sigma_{zz}\sigma_{xx} - \sigma_{xz}\sigma_{zx} \end{aligned} \quad (3.50)$$

as $\sigma_{xy} = \sigma_{yz} = 0$. After some algebra:

$$q = \sqrt{\sigma_{xx}^2 + \sigma_{yy}^2 + \sigma_{zz}^2 - \sigma_{xx}\sigma_{yy} - \sigma_{yy}\sigma_{zz} - \sigma_{zz}\sigma_{xx} + 3\sigma_{xz}^2} \quad (3.51)$$

And upon substitution of the wave-induced stresses into (3.46) we find for the total deviatoric stress q and its amplitude \hat{q} , including the isotropic part:

$$\begin{aligned} q &= \sqrt{3} \left(p_w^2 k^2 z^2 e^{-2kz} + p_w k z e^{-kz} \cos(\omega t - \varphi) (1 - K_0) \left(\int_z \rho_{dry} g dz' \right) + \right. \\ &\quad \left. + \frac{1}{3} \left((1 - K_0) \int_z \rho_{dry} g dz' \right)^2 \right)^{1/2} \end{aligned} \quad (3.51a)$$

$$\begin{aligned} \hat{q} &= \sqrt{3} \left(p_w^2 k^2 z^2 e^{-2kz} + p_w k z e^{-kz} (1 - K_0) \left(\int_z \rho_{dry} g dz' \right) + \right. \\ &\quad \left. + \frac{1}{3} \left((1 - K_0) \int_z \rho_{dry} g dz' \right)^2 \right)^{1/2} \end{aligned} \quad (3.51b)$$

Note that the dry bed density is kept constant, so that $\rho_{dry}(x, y, z, t) = \rho_m = \text{const}$. The initial effective (isotropic) stress p_0 prior to liquefaction follows from substitution of (3.41) into (3.49):

$$p_0 = \frac{1}{3} (\sigma_{xx} + \sigma_{yy} + \sigma_{zz})_0 = \frac{2K_0 + 1}{3} \int_z \rho_{dry} g dz' \quad (3.53)$$

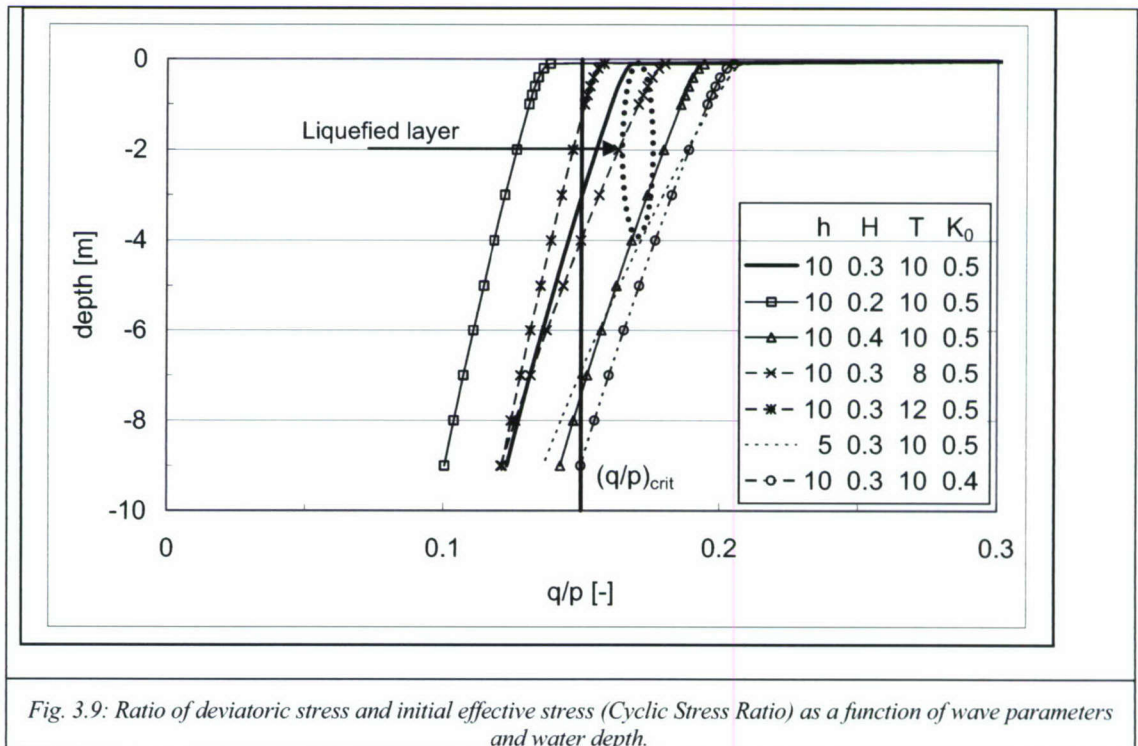
Hence, we have derived simple explicit formula for the deviatoric and isotropic stress varying with depth z into the seabed as a function of wave characteristics; at depth $z = z_{crit}$, the inequality of relation (3.48) is met, and the bed fails. We assume that all sediment above z_{crit} becomes liquefied and behaves as a fluid. Hence, z_{crit} defines the thickness δ of the fluid mud layer in the 2L model.

The stress history of the bed, which can be quantified with the Over Consolidation Ratio (OCR) can be modeled through α (equ. (3.48)). However, in the cases we are interested, at which the fluid mud layer liquefies and regains strength frequently, the OCR will be close to unity in general.

In case of irregular waves, a preliminary inspection of the wave spectrum is necessary to assess which part of the spectrum is relevant for the liquefaction of the mud bed. This is in particular the case when the spectrum contains two peaks, with a first peak generated by

swell and a second peak generated by local wind. In general, the longer waves will be the more relevant for the liquefaction of the waves. It is not obvious which wave conditions are critical for liquefaction – this may vary from site to site, and possibly even at a particular site. The larger waves generate the largest stresses, but do not occur frequently. Smaller waves generate smaller stresses, but occur more frequently. Therefore, we anticipate that the mean wave height and corresponding wavelength and period are the dominant waves with respect to liquefaction.

As an example, the CSR is plotted in Fig. 3.9 for various wave characteristics. We have also plotted a hypothetical critical stress ratio $(\hat{q}/p)_{crit}$, assuming that all the mud above the level where the actual stress level exceeds said critical value becomes liquefied. As we assume that liquefaction takes place in a time period which is short compared to the overall storm period, we are not concerned with the time necessary for liquefaction, i.e. we do not take into account the number of wave cycles. The critical stress ratio $(\hat{q}/p)_{crit}$ has to be assessed experimentally, i.e. through cyclical triaxial tests.



3.6 Strength evolution and the rheological model

The non-Newtonian behavior of the mud is described with a Bingham model in the 2L FLUID MUD MODEL (e.g. equ. (3.5) and (3.6)). Therefore we propose to extend the Bingham model to account for the effects of waves and thixotropy. The general formulation of the Bingham model is given by Malvern (1969) and reads for stresses/strains in the vertical plane:

$$T'_{iz} = \left(2\mu + \frac{\tau_B}{\sqrt{\Pi_D}} \right) D_{iz} \quad , i = x, y \quad ; \quad T'_{iz} \geq \tau_B \quad (3.54)$$

where T'_{iz} = deviatoric stress tensor, μ = dynamic viscosity, τ_B = Bingham yield strength, D_{iz} = rate of deformation tensor, and Π_D = second invariant of D_{iz} ; we have assumed $T'_{xy} \approx D_{xy} \approx 0$. Next, we assume that D_{iz} consists of a contribution by flow-induced deformation (superscript f) and wave-induced deformation (superscript w), and that these effects can be superposed linearly: $D_{iz} = D_{iz}^f + D_{iz}^w$.

Furthermore, we introduce a structure parameter to account for thixotropic effects, i.e. the muddy seabed experiences repetitive liquefaction under wave action and strength recovery under calm weather conditions. Our approach is based on Moore (1959), who proposed a simple model to describe such thixotropic effects through a structure parameter λ_s (see also Coussot, 1997). This model can be extended (Winterwerp, 1993, see also Toorman, 1997) by incorporating this structure parameter also in the yield strength, which reads for stresses in one vertical plane only:

$$\tau = \tau_{B,\infty} + \lambda_s \tau'_B + (\mu_\infty + \lambda_s \mu') \dot{\gamma} \quad (3.55)$$

where τ'_B = yield (Bingham) strength parameter, $\tau_{B,\infty}$ = residual yield strength for fully deflocculated sediment, μ_∞ = viscosity for fully deflocculated sediment, μ' = a viscosity parameter, and $\dot{\gamma}$ = shear rate. The structure parameter $\lambda_s = 1$ for fully flocculated sediments (all bonds active) and $\lambda_s = 0$ for fully deflocculated sediment (all bonds destroyed). This behavior is depicted schematically in Fig. 3.10.

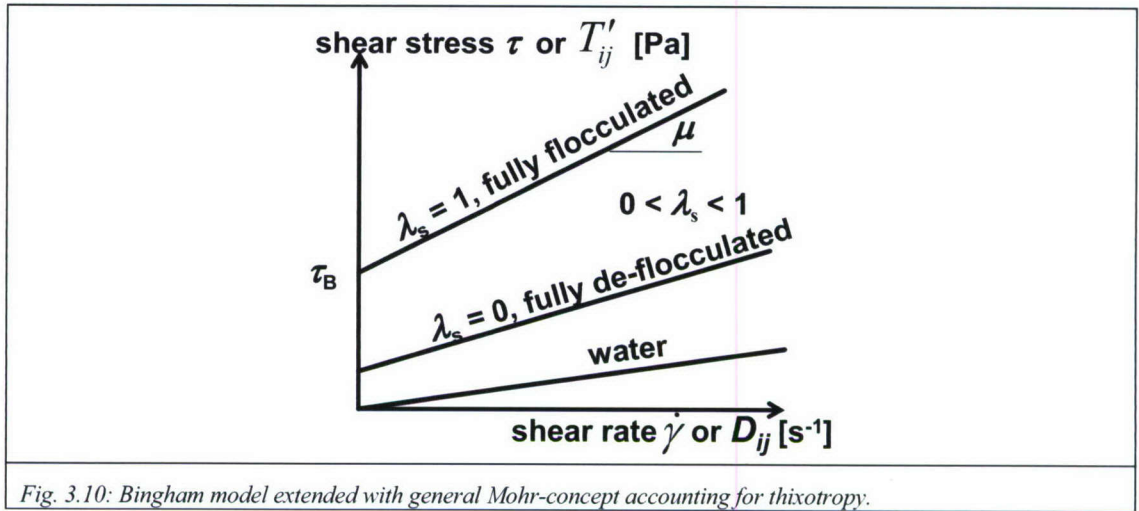


Fig. 3.10: Bingham model extended with general Mohr-concept accounting for thixotropy.

Combining these ingredients yields:

$$\tau_{iz} = \mu_{eff} (D_{iz}^f + D_{iz}^w) \quad (3.56)$$

in which the effective viscosity μ_{eff} is given by:

$$\mu_{eff} = \frac{\tau_{B,\infty} + \lambda_s \tau'_B}{\sqrt{\Pi_D}} + \mu_\infty + \lambda_s \mu' \quad (3.57)$$

The flow- and wave-induced rates of deformation are then given by:

$$D_{iz}^f = \frac{\partial u_i}{\partial z} \quad \text{and} \quad D_{iz}^w = \frac{\hat{q}_i}{\mu_{eff}} \quad (3.60)$$

where \hat{q}_i is the wave-induced deviatoric stress component in x - or y -direction (e.g. equ. (3.46), (3.47) and (3.51b)).

By similar arguments, we scale the soil mechanical parameters with the structure parameter as well, so that as well the cohesion c and the angle of internal friction ϕ become:

$$c = \lambda_s c_0 \quad \text{and} \quad \phi = \lambda_s \phi_0 \quad \text{hence} \quad K_0 = 1 - \sin(\lambda_s \phi_0) \quad (3.59)$$

This thixotropic model can be used to establish the viscosity and stress terms in the momentum equation of the 2L FLUID MUD MODEL, e.g. equ. (3.5). Generally, the fluid mud flow will be laminar. This implies that the friction coefficient λ (equ. (3.6) and (3.7)) scales linearly with viscosity, i.e. we assume:

$$\lambda = k_\lambda \frac{\mu_\infty + \lambda_s \mu'}{\delta \sqrt{(u_m^L)^2 + (v_m^L)^2}} \quad (3.60)$$

In which k_λ is a coefficient to be tuned (from laminar flow theory, $k_\lambda = 64$, so we anticipate $10 < k_\lambda < 100$). Furthermore, the viscosity and Bingham strength in equ. (3.5) and (3.6) read:

$$\nu = (\mu_\infty + \lambda_s \mu') / \rho_m \quad \text{and} \quad \tau_B = \tau_{B,\infty} + \lambda_s \tau'_B \quad (3.61)$$

Note that the viscosity ν is also used in the wave-damping module in SWAN – see Section 3.3.

The rate of flocculation is given by Moore (1959):

$$\frac{d\lambda_s}{dt} = a(1 - \lambda_s) - b\lambda_s \sqrt{\Pi_D} \quad (3.61)$$

where a and b are flocculation and floc break-up parameters, to be determined empirically. Toorman (1997) found from roto-viscometer tests ($\sqrt{\Pi_D} = \dot{\gamma}$) values of $a = O\{10^{-2}\} \text{ s}^{-1}$ and $b = O\{10^{-4}\}$. This implies a very rapid response of the seabed to changes in forcing conditions. This will have to be verified for the conditions under consideration, but most likely the time scales will be considerably larger.

Finally, we have to elaborate (3.54) for the 2L FLUID MUD MODEL. This implies that we have to integrate the wave-induced deviatoric stress \hat{q} over the mud layer thickness δ : $\hat{Q} = \int_{\delta} \hat{q} dz$. Then Π_D , both in equ. (3.57) and (3.61) becomes:

$$\Pi_D = \left(\frac{\hat{Q}}{\mu_{eff}} \right)^2 + \left(\frac{u_m}{\delta} \right)^2 + \left(\frac{v_m}{\delta} \right)^2 \quad (3.63)$$

It is noted that the denominator of (3.57) becomes zero when $\hat{Q} = u_m = v_m$, so this will have to be implemented accurately in the numerical code.

The material parameters a and b have to be established from rheological experiments, for instance through cyclical triaxial tests. We note that from small scale experiments, the time-scale for recovery appears to amount of the order of (a fraction) of seconds. This seems unrealistically fast. However, from experience with larger samples, strength recovery is expected to take place within a period of the order of hours up to a day at most.

4 Implementation into the 2L FLUID MUD MODEL

The cycle of liquefaction, traction and strength recovery is sketched in Fig. 4.1a – d. At $t = 0$ (i.e. initial model conditions) a maximum liquefiable mud layer is defined by the user with spatial varying thickness $\delta_{\max}(x,y;t=0)$. This mud layer has the properties of the fully flocculated material, i.e. $\lambda_s = 1$ (e.g. Fig. 4.1a). Then, when waves arrive at the relevant domain, all or part of the liquefiable mud gets liquefied, and the liquefied mud with extension $\delta_m(x,y;t=t_1)$ attains the properties of the fully deflocculated material, i.e. $\lambda_s = 0$ (e.g. Fig. 4.1b.). Next, the liquefied mud is transported by the wave stresses, as sketched in Fig. 4.1c ($t = t_2$). Then, strength is recovered, $\lambda_s = 1$ again, and a new spatial distribution of liquefiable mud is obtained (e.g. Fig. 4.1d, $t = t_3$).

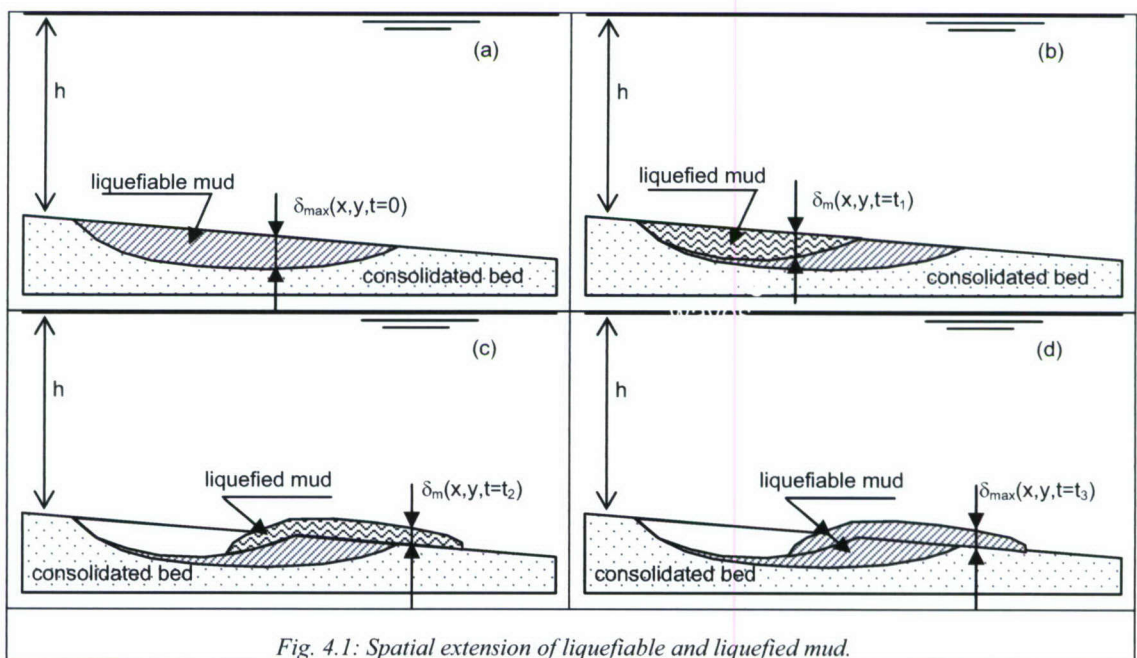


Fig. 4.2 presents the flow scheme of the new 2L FLUID MUD MODEL.

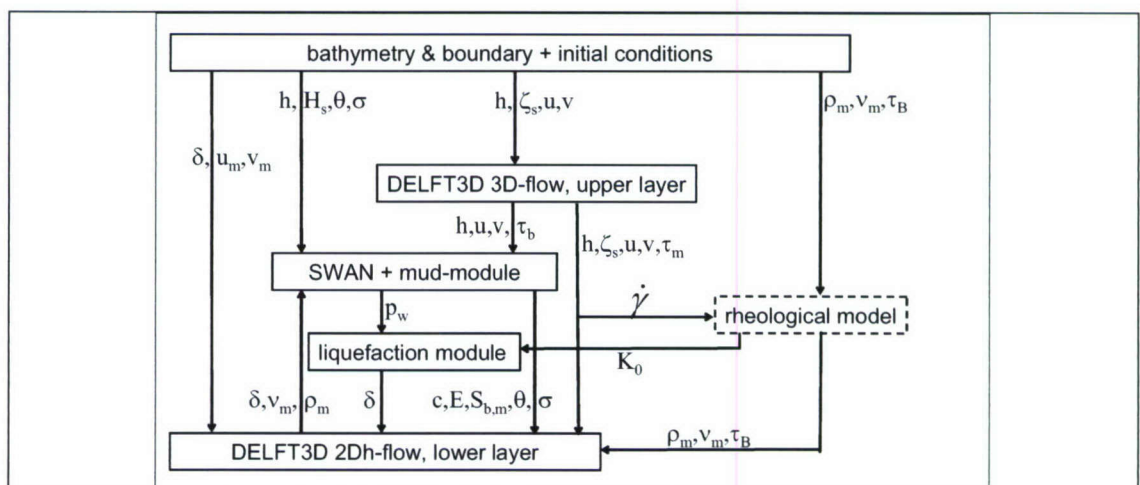


Fig. 4.2: Flow scheme of 2L FLUID MUD MODEL.

Finally, we repeat Table 2.1 describing the phasing of the model development.

Table 4.1: Phasing of the model set-up.

Phase	physical process	for the given parameters	physical	see Sections
1	mud-induced wave damping	$\delta(x,y), \mu, \tau_B, \rho_m$		3.3 & 5
2	wave-induced mud transport	$\delta(x,y), \mu, \tau_B, \rho_m$		3.4 & 6
3	wave-induced liquefaction	μ, τ_B, ρ_m		3.5 & 7
4	strength recovery after storm	ρ_m		3.6

5 Application mud-induced wave damping

5.1 Validation against laboratory experiments

De Wit (1995) carried out wave damping experiments in a 40 m long wave and flow flume, with a width and depth of 0.8 m. A false floor was mounted on the flume bottom to create a 0.2 m deep test section of 8 m length in which a dense mud suspension could be placed. Regular waves were generated with a wave paddle. During the experiments wave height and period were measured, together with vertical profiles of the flow velocity and suspended sediment concentration at a number of places, and the total and pore water pressure at four heights within the dense mud suspension.

Dense mud beds were formed in the test section through consolidation of more dilute mud slurries. In this report we use De Wit’s experiment III, test 3, carried out with China clay (major mineral component consists of kaolinite) to validate the wave damping module in SWAN. A slurry of China clay was prepared in a tank by mixing clay powder with fresh tap water in which 0.5% sodium chloride was dissolved, yielding a sediment concentration of about 275 kg/m³. After a consolidation time of six days the concentration increased to about 500 kg/m³, i.e. to a density of about 1300 kg/m³. The viscosity of this suspension measured about 2.7·10⁻³ m²/s, i.e. about 300 times larger than that of water. Though, the strength of the mud has not been measured, it is estimated at about the liquid limit.

Prior to test 3, two other tests were carried out. During test 1, only waves were generated with a height of 22 mm, whereas during test 2 also a net flow occurred (velocities of 5, 10 and 15 cm/s) at a wave height of 38 mm. Then the bed was left at rest for another day upon which test 3 was carried out with waves of 45 mm, but no current.

Fig. 5.1 shows the measured variation of wave height at six locations along the flume after equilibrium was attained. It is shown that the wave height at the end of the test section has decreased to about 35 mm, i.e. a reduction by about 20%.

Next, the new SWAN mud wave damping model was used to simulate these measurements. The model parameters were obtained from the measurements by De Wit (1995); De Wit and Kranenburg (1997) and are summarized in Table 5.1.

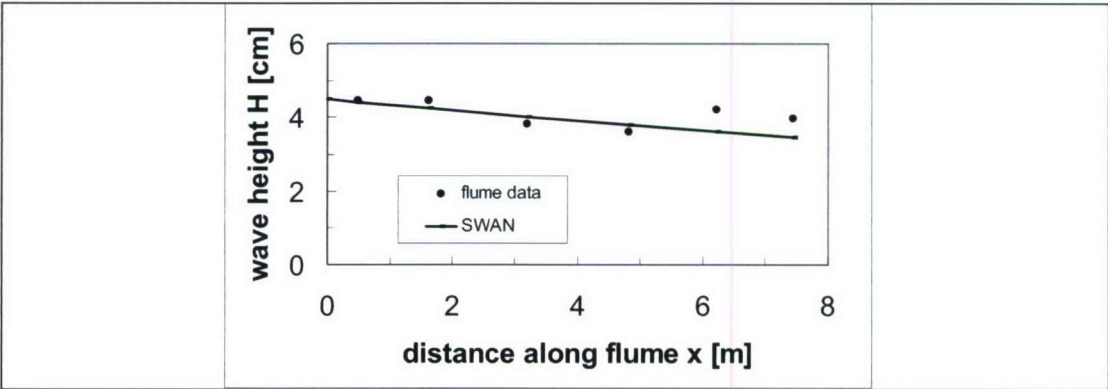


Fig. 5.1. Comparison of measured and computed wave height in laboratory flume.

The results of the SWAN-simulations are also presented in Fig. 5.1, showing a favorable agreement between the experimental data and the numerical simulations.

Table 5.1
mud parameters in SWAN mud wave damping model (after De Wit, 1995).

ρ_w [kg/m ³]	ρ_m [kg/m ³]	$\delta_{m,0}$ [m]	h_0 [m]	H [m]	ν_m [m ² /s]	α
1000	1300	0.115	0.325	0.045	$2 \cdot 6 \cdot 10^{-3}$	1

5.2 Application to Guyana coast

5.2.1 Observations

Fig. 5.2 shows an aerial photograph of the breaker zone at Demerara coast of the Guyana coastal system. Towards the west (right-hand part of the photo) white bands of foam, characteristic for wave breaking, are clearly visible. Further to the east, no foam is visible; in fact hardly any waves can be observed.

However, no detailed wave data in the Guyana coastal system are available at present from which the wave attenuation over the muddy seabed can be assessed quantitatively. Only some general data have been reported by NEDECO (1972) on decreases in wave heights under average conditions from 1.3 to 0.3 m and under extreme conditions from 4 to 1.2 m.

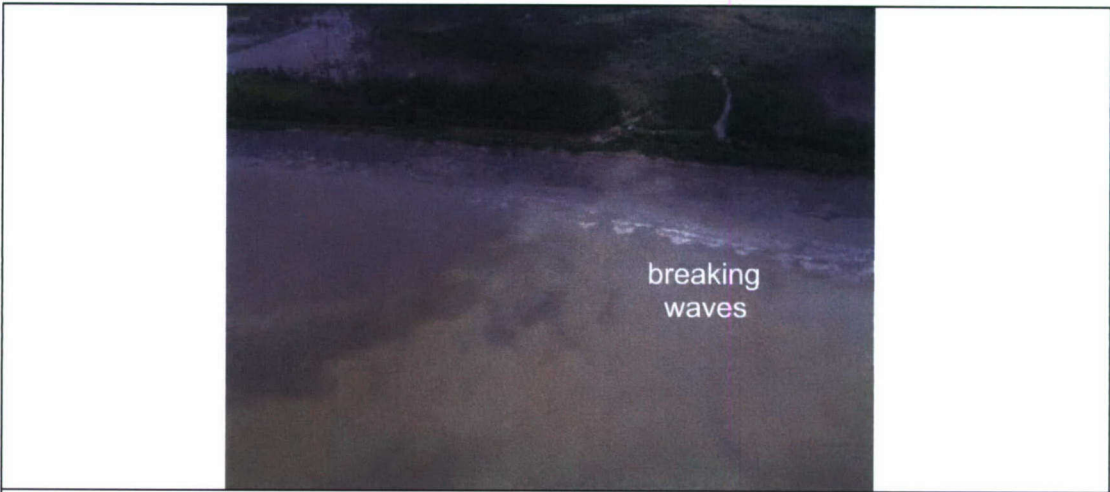


Fig. 5.2: Aerial photograph of wave braking and wave damping at Guyana, Demerara coast.

A good qualitative picture can be obtained from data a similar site though. Fig. 5.3 depicts the measurements by Wells and Coleman (1986) of wave spectra at three locations in the Surinam coastal waters. The spectra consist of two parts: a strong peak at $T_w = 9 - 10$ s, where T_w is the wave period, reflecting energy in the swell from the Atlantic Ocean and a wider band between $T_w = \sim 2$ and ~ 5 s, reflecting the energy in locally generated waves. The total wave energy has dissipated by about 88% at the middle measuring station (i.e. over a distance of about 9 km) and for 96% at the most near-shore station. Note the difference in vertical scale in the graphs. The conditions at Surinam coast are so similar to those at the

Guyana coastal, that it is believed that the observations of Fig. 5.3 are characteristic for the Guyana coastal system as well.

As explained before, the strong wave attenuation shown in Fig. 5.2 and 5.3 is expected to be caused by viscous dissipation in the liquefied seabed. Unfortunately, up till now we have no direct measurements of such liquefaction, and we have to rely on physical interpretation of other data. Fig. 5.6 shows the filtered results of recent dual frequency echo soundings along a cross section perpendicular to Guyana coast. The upper signal (210 kHz) reflects the top of the soft mud bed, whereas the lower signal (33 kHz) reflects some of the structure within the bed. This graph reveals a small pool of fluid mud only, depicted by the gap between the two signals at around $x = 8000$ m. The irregularity of the lower frequency echo signal is typical for layered mud deposits. This is further depicted in Fig. 5.5, showing reflections from a 20 kHz sub-bottom profiler applied by Delft Hydraulics Laboratory (1962) in the vicinity of Demerara river mouth. The multiple reflections are typical for stratified mud deposits; the thickness of the layers is estimated at about 1 – 2 dm (the vertical resolution is not known unfortunately, but can be estimated from the amplitude of the wavy acoustic signal³⁾). This layered structure cannot be caused by sedimentation events, as the sedimentation rate in the Guyana coastal system is not driven by episodic events. Hence, this stratification can only be caused by frequent, incomplete liquefaction of the seabed.

³⁾ These small acoustic waves are marked by an ellipse in Fig. 5.5. Their amplitude a follows from $a = c/f$, where c is the speed of sound in the seabed ($c \approx 1500$ m/s) and f is the frequency of the acoustic wave ($f = 20$ kHz). Hence, $a \approx 7.5$ cm.

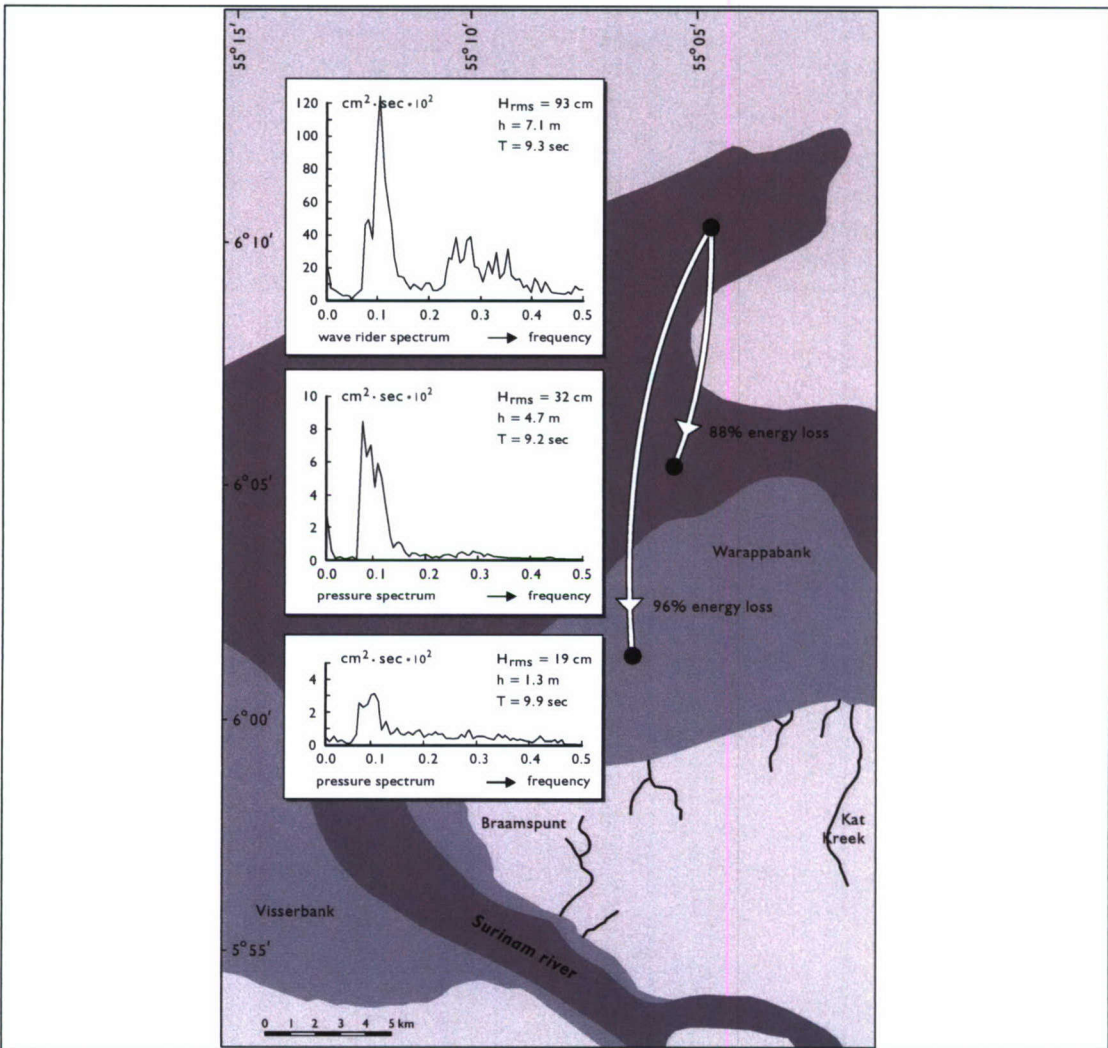


Fig. 5.3: Wave attenuation measured in Surinam coastal system (after Wells and Coleman, 1986).

From this analysis we deduce from Fig. 5.4 and 5.5 that the thickness of the liquefiable bed amounts to about 2 m, and we infer that we can assess the thickness of the fluid mud layer and its extension from spatial data on the echo-soundings.

The in-situ density has been measured by NEDECO (1972). They found values for ρ_m ranging from 1300 to 1500 kg/m³. As variations in density cannot be very large, and as the dissipation function is not very sensitive to small variations in density, we take an average value of $\rho_m = 1400$ kg/m³.

Some viscosity measurements have been carried out by NEDECO (1972), as well, with ranges between $\eta = 0.1 - 10$ Pa.s. As these data are not very accurate, the viscosity is our main calibration parameter.

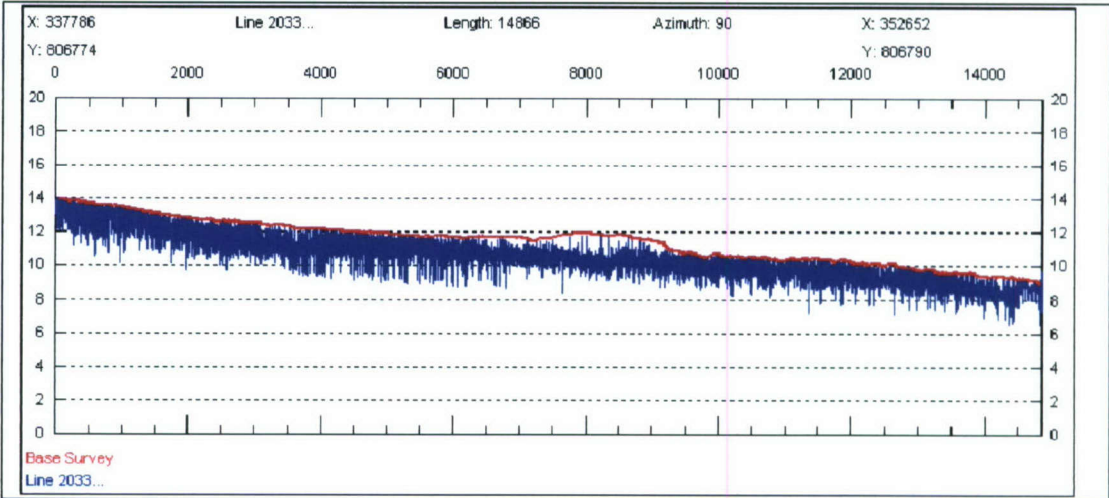


Fig. 5.4: Filtered acoustic reflections from dual frequency echo sounding ($f = 210$ & 33 kHz) along a cross section in Guyana coastal system perpendiculars to the coast.

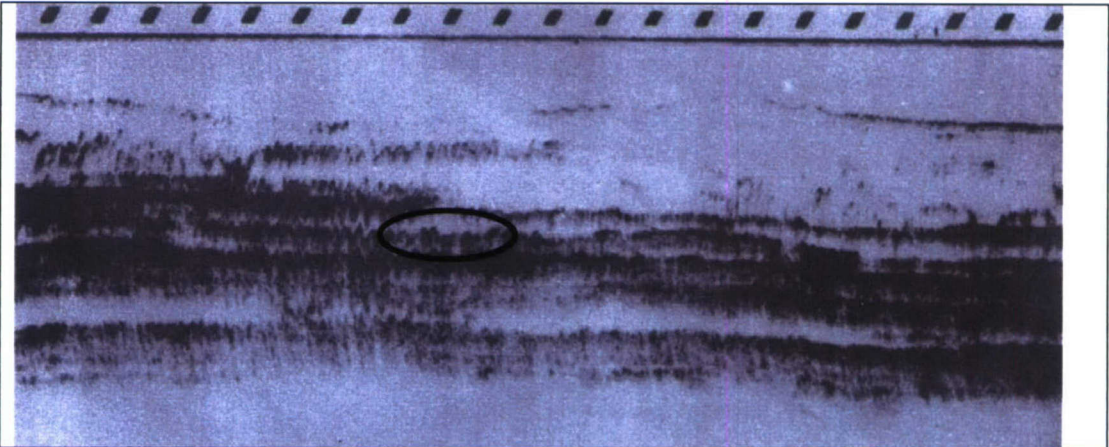


Fig. 5.5: Acoustic reflections from sub-bottom profiling ($f \approx 20$ kHz) in Guyana coastal system, Demerara mouth (Delft Hydraulics Laboratory, 1962) – the vertical scale is not known, but estimated at about 0.5 m.

5.2.2 Simulations

The modified SWAN-model (as described in Chapter 3) is applied to the wave model covering a large part of the Guyana coastal system, including the Essequibo estuary (see Fig. 5.6). The model covers a 250 km wide coastal area and extends about 85 km offshore. The depth at the offshore boundary of the model varies between 135 to 40 m.

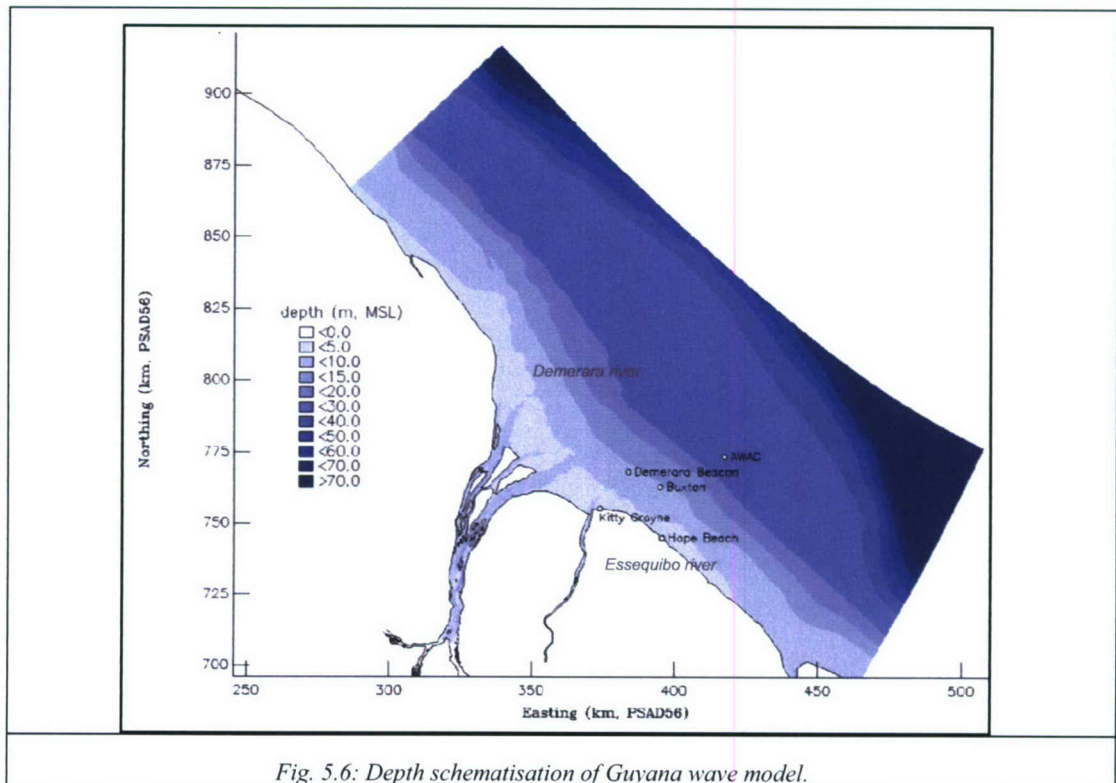


Fig. 5.6: Depth schematisation of Guyana wave model.

The wave model employs a curvilinear grid that comprises 263 by 383 points, with approximately 42,000 active points. This computational grid is presented in Fig. 5.7. The dimensions of the grid cells vary from 2.5 km near the model boundaries to approximately 200 m in the Essequibo estuary, near Georgetown and in the nearshore zone.

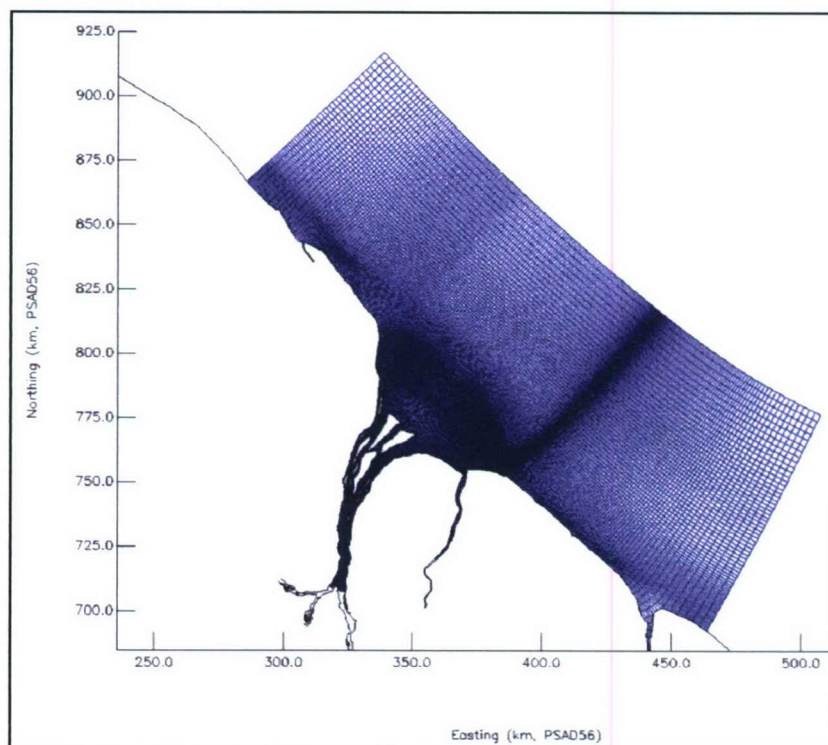


Fig. 5.7. Computational curvilinear grid of Guyana Wave model.

Considering the presence of relatively long waves, the width of the energy distribution was taken at $ms = 10$ (instead of $ms = 4$ in case of wind-generated waves) in the wave model. For the wave spectrum a directional resolution of 10° was adopted over the full circle. The frequency spreading was schematised using 31 discrete frequencies between 0.05 Hz and 1 Hz using a logarithmic scale. For the remaining parameters the default settings of the SWAN model were used.

The SWAN mud wave damping model requires as input the thickness of the (fluid) mud layer in the model area. This was defined as the difference between the high frequency echo reflections and the lowest 10% of the low frequency echo reflections (see Fig. 5.4). The resulting spatial varying mud layer thickness varying between 1 m and 5.5 m, as indicated in Fig. 5.8.

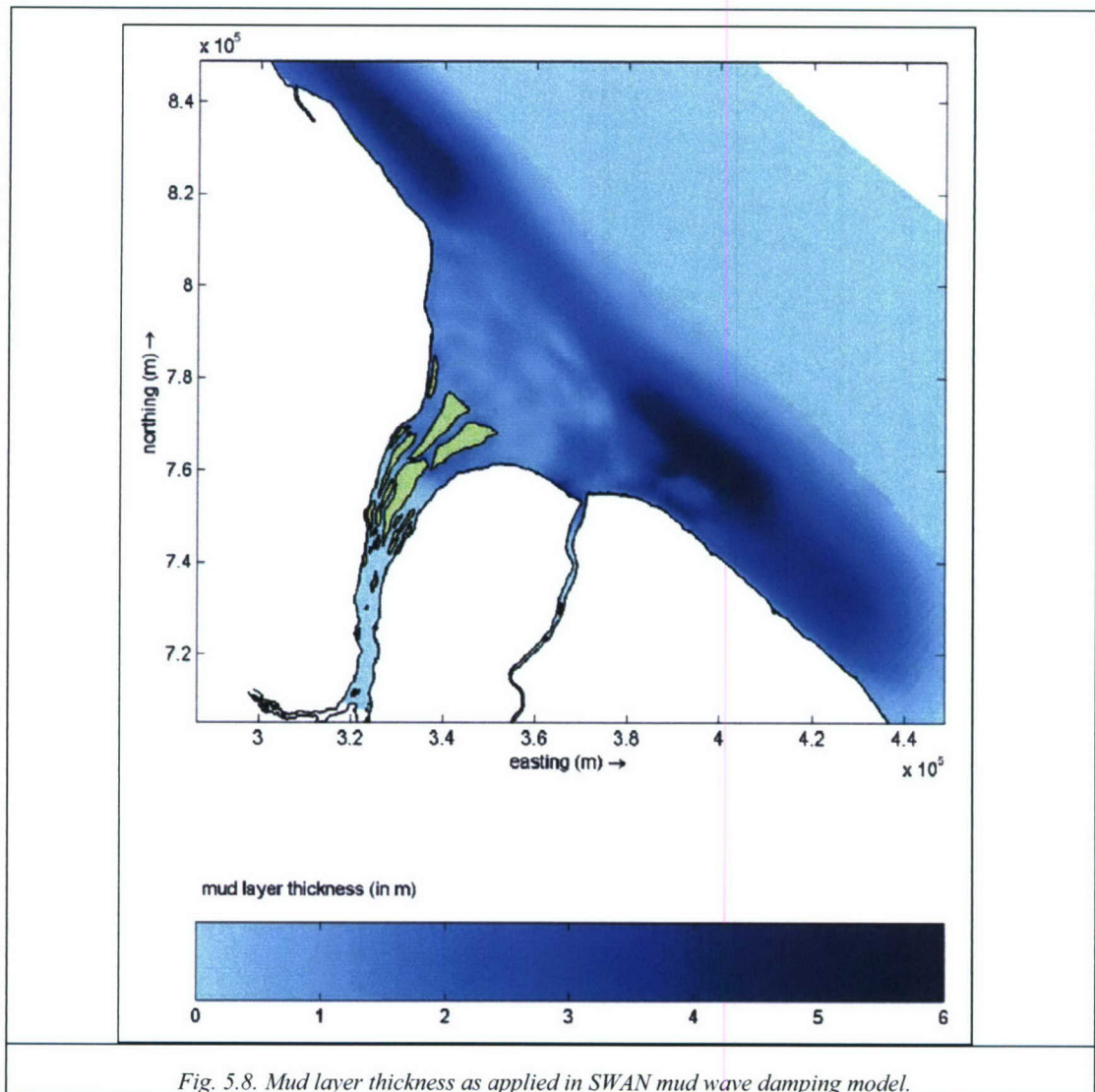


Fig. 5.8. Mud layer thickness as applied in SWAN mud wave damping model.

The model is calibrated on the basis of a comparison of average wave heights observed at three nearshore locations, as presented in NEDECO (1972). The observation locations are indicated in Figure 5.6. The objective of the calibration is to optimise the settings of the input variables of the SWAN mud wave damping model. A further calibration of the model on the basis of simultaneous offshore and nearshore measurements is not possible as no simultaneous nearshore wave measurement data are available at present.

In NEDECO (1972) average and maximum wave heights at three nearshore and one offshore locations are presented. Considering the dynamic behaviour of the (mud) bed at the location of the nearshore observations, it is very likely that the current seabed differs from the seabed at the time the observations were made. Consequently, it is not possible to make a direct comparison between the nearshore observations and model results (based on the current bathymetry). It is therefore not possible to accurately represent these observations. However, we require them to be of the same order of magnitude as an indication to whether the damping of the wave energy is properly represented by the SWAN mud wave damping model.

As no detailed information was available on the characteristics of the fluid mud itself, the mud parameters had to be assessed from literature or sensitivity analyses. We kept the density of the fluid mud constant, as this is expected not to vary too much. The mud's viscosity is determined by trial-and-error and is thus basically a calibration factor. The selected values are given in Table 5.2. Computations were carried out with $\nu_m = 0.01, 0.001$ and $0.0001 \text{ m}^2/\text{s}$.

Table 5.2
Input parameters and settings for the SWAN mud wave damping model.

Parameter	settings
thickness of the fluid mud layer δ_m	spatially varying on computational grid [m]
density of fluid mud, ρ_m	1400 kg/m ³
density of water, ρ_w	1010 kg/m ³ (at $T = 25^\circ\text{C}$ and $S = 20$ ppt)
viscosity of fluid mud, ν_m	calibration parameter [m ² /s], ranging between 0.01 and 0.0001 m ² /s
calibration parameter, α	1.0 [-]

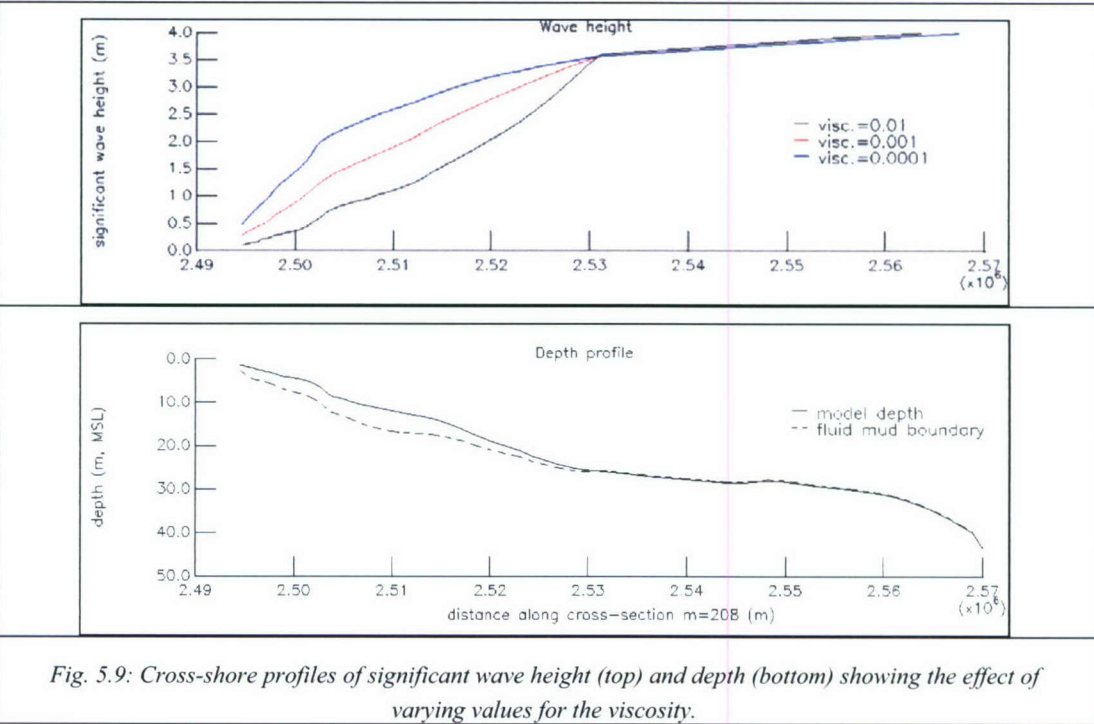
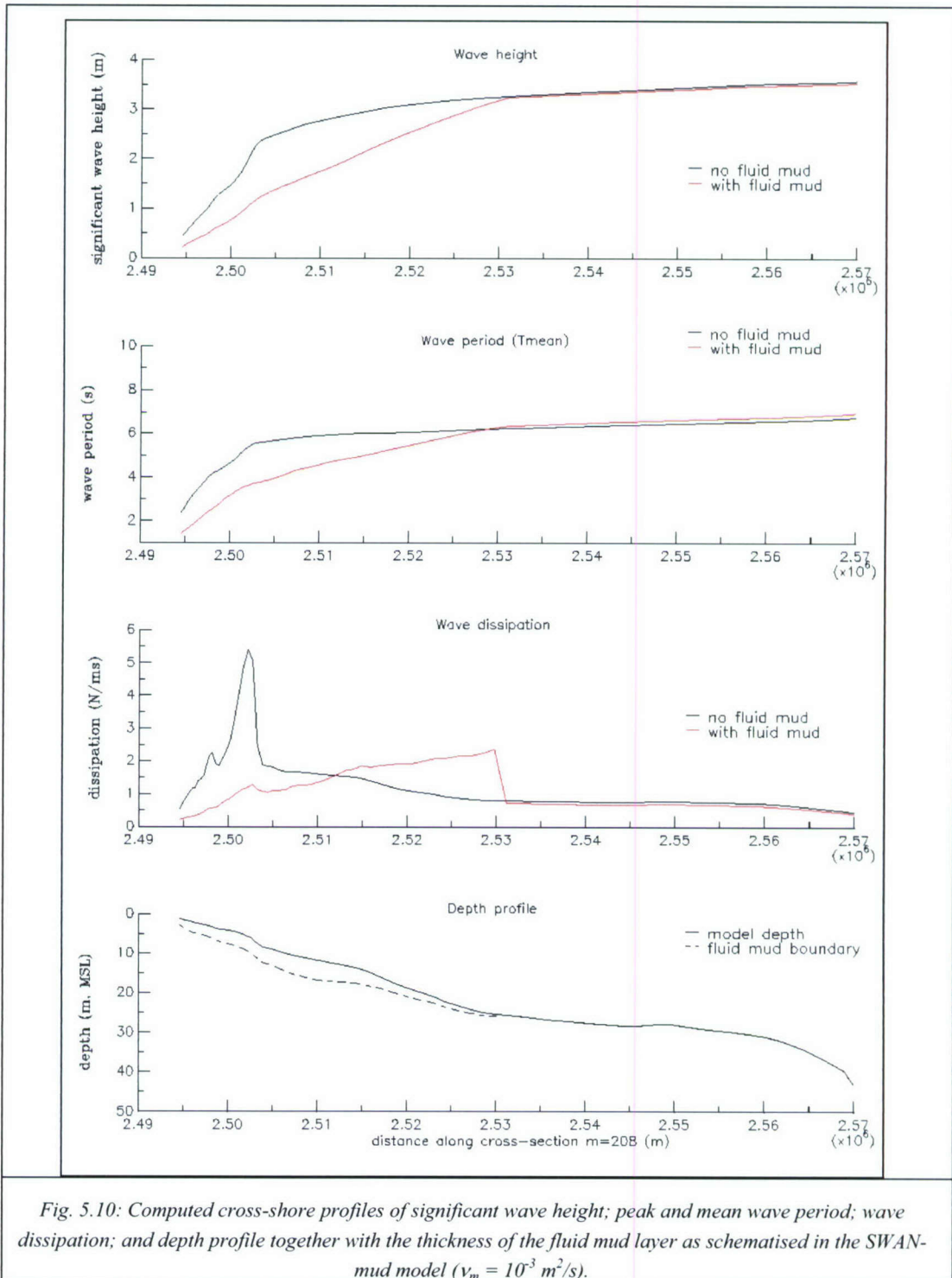


Fig. 5.9: Cross-shore profiles of significant wave height (top) and depth (bottom) showing the effect of varying values for the viscosity.

The effect of the varying ν_m during an extreme wave condition ($H_{m0} = 4 \text{ m}$, $T_p = 10 \text{ s}$ accompanied by a NE wind of 12.5 m/s) on the significant wave height is presented in Fig. 5.9. This figure shows cross-shore profiles (approximately located at Hope Beach, see Fig. 5.6) of the significant wave height and depth profile as well as the thickness of the fluid mud

layer as schematised in the SWAN model. It shows that the mud's viscosity has an important effect on the wave attenuation.



In our further analyses we apply $\nu_m = 10^{-3} \text{ m}^2/\text{s}$ (i.e. $\eta_m = 1.3 \text{ Pa}\cdot\text{s}$), as this value gave the best results; moreover, this is a typical value for muddy beds at the observed densities. The effect of fluid mud-induced wave damping in the wave computations is shown in Figure 5.10 for an extreme wave conditions from the ENE direction. This figure presents cross-shore profiles of the significant wave height (H_{m0}); peak and mean wave period (T_p and

T_{m01}); wave dissipation ($S'_{b,m}$); and depth profile and thickness of the fluid mud layer (h_0 and $\delta_{m,0}$) as schematised in the model. Figure 5.9 shows that:

The mean wave period decreases strongly over the fluid mud layers, with a stronger dissipation of the low-frequency waves;

The wave heights start to decrease a about 25 m water depth with a relative decrease up to 50% at about 5 m water depth when taking into account wave damping by fluid mud;

The dissipation of wave energy starts at the offshore end of the fluid mud layer and is fairly constant towards the coast. In case wave damping by fluid mud is not included in the wave model, a peak in wave dissipation is found at the coastline, where the waves break due to depth limitation. The latter not being observed at the area of interest of Guyana coastal system.

The effect of wind-generated waves on the wave climate is illustrated in Fig. 5.11 showing one-dimensional wave spectra at three locations for an extreme wave condition ($H_s = 4$ m) from the NE direction. The simulation includes wave damping by fluid mud. Note the growth of wind-generated waves (at a frequency of about 0.2 Hz) towards the coast and the dissipation of the swell (at a frequency of about 0.1 Hz). In this case the peak period shifts from 10 s offshore to 5 s at a nearshore location. The energy of the > 0.2 Hz waves reduces by a factor 3 from A to B, and at their peak by a factor 5.10. This uneven behaviour in dissipation is owing to the effects of bed friction and/or viscous dissipation in the mud layer. The latter effect, however, is by far the larger of the two (e.g. Fig. 5.10). This process of wave attenuation towards the coast agrees qualitatively with the measurements by Wells and Coleman (1986), see Fig. 5.3.

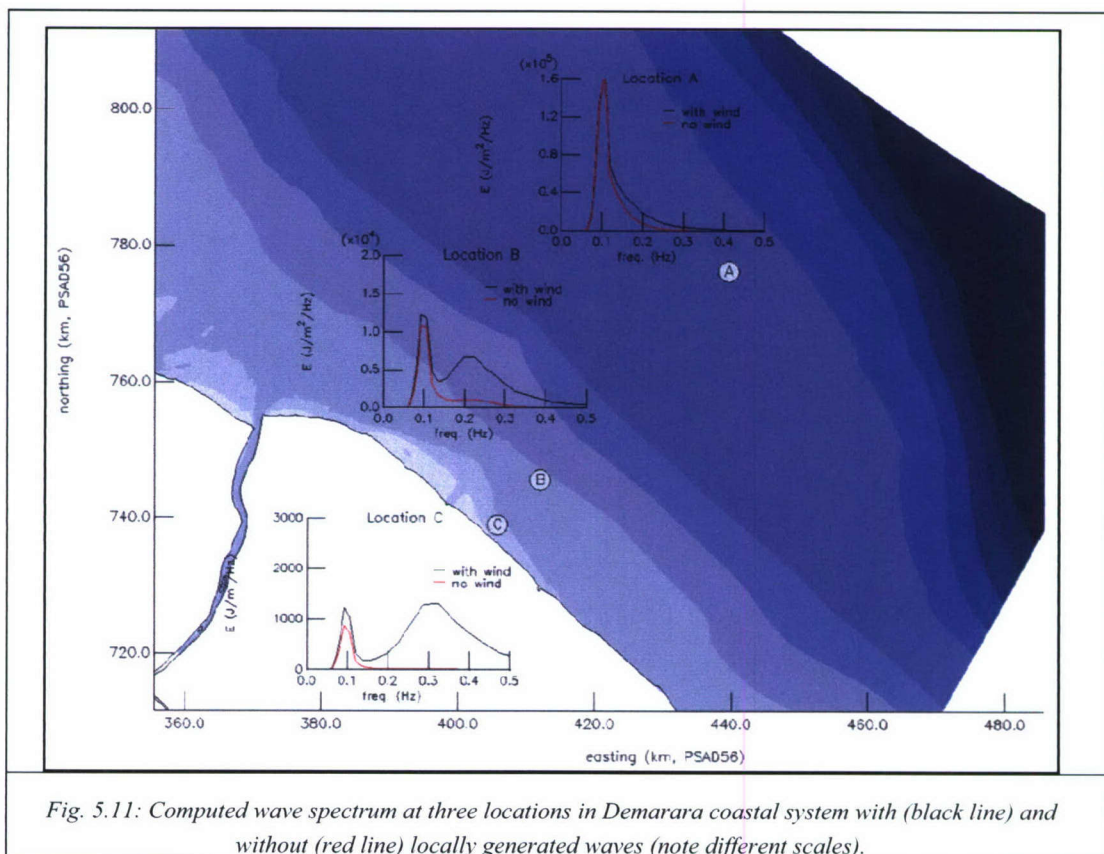


Fig. 5.11: Computed wave spectrum at three locations in Demarara coastal system with (black line) and without (red line) locally generated waves (note different scales).

Table 5.3 presents the comparison between historical nearshore observations described in NEDECO (1972) and the model results with and without the fluid mud-induced wave

damping. Here it is concluded that when including the SWAN mud wave damping model (with the above variable settings), the damping effect of the wave energy is in reasonable agreement with the observations. Wave heights are significantly being overestimated in case fluid mud-induced wave damping is not included in the SWAN simulations.

Table 5.3
Comparison between historical observations (NEDECO, 1972) and model results with $\square_m = 0.001 \text{ m}^2/\text{s}$.

Location	observed H_s [m]	Computed H_s [m] with fluid mud	Computed H_s [m] without fluid mud
Average wave conditions			
Offshore	1.3	1.3	1.3
Buxton	0.6	0.6	1.0
Demerara	0.5	0.6	1.0
Beacon			
Kitty Groyne	0.3	0.1	0.5
Maximum wave conditions			
Offshore	4.0	4.0	4.0
Buxton	2.0	1.6	2.9
Demerara	1.3	1.5	2.8
Beacon			
Kitty Groyne	1.2	0.4	0.9

6 Application of wave-induced mud transport

Sakakiyama and Bijker (1987) describe experiments in a horizontal wave flume, measuring both mud-induced wave damping and wave-induced mud transport. A bed of kaolinite and fresh water was placed in a test section in between two wooden false floors. The test section was 12 m long and the mud thickness amounted 0.095 m, whereas the flume was 0.5 m wide. Mud beds with a density varying between 1140 and 1380 kg/m³ were prepared. Wave heights were varied between 1 and 4.4 cm, at wave periods varying between 0.6 and 2 s. The water depth was kept constant at 0.3 m.

Sakakiyama and Bijker (1987) measured surface wave height and attenuation, the height of the water-mud interface, and the velocity within the mud layer. Also, viscosity and strength of the mud layer were established independently.

The series at the highest mud density are most interesting as they show considerable wave damping at higher wave heights and ditto mass transport in the first part of the mud bed, whereas in the second part of the mud bed, waves are damped so much that liquefaction nor mass transport was measured. This is depicted in Fig. 6.1, showing for the higher initial wave height damping over the first 7 m of the test section, where after the wave height remains constant at about 1 cm. When the initial wave height amounted to 1 cm, no damping occurred; apparently, the mud bed could not be liquefied.

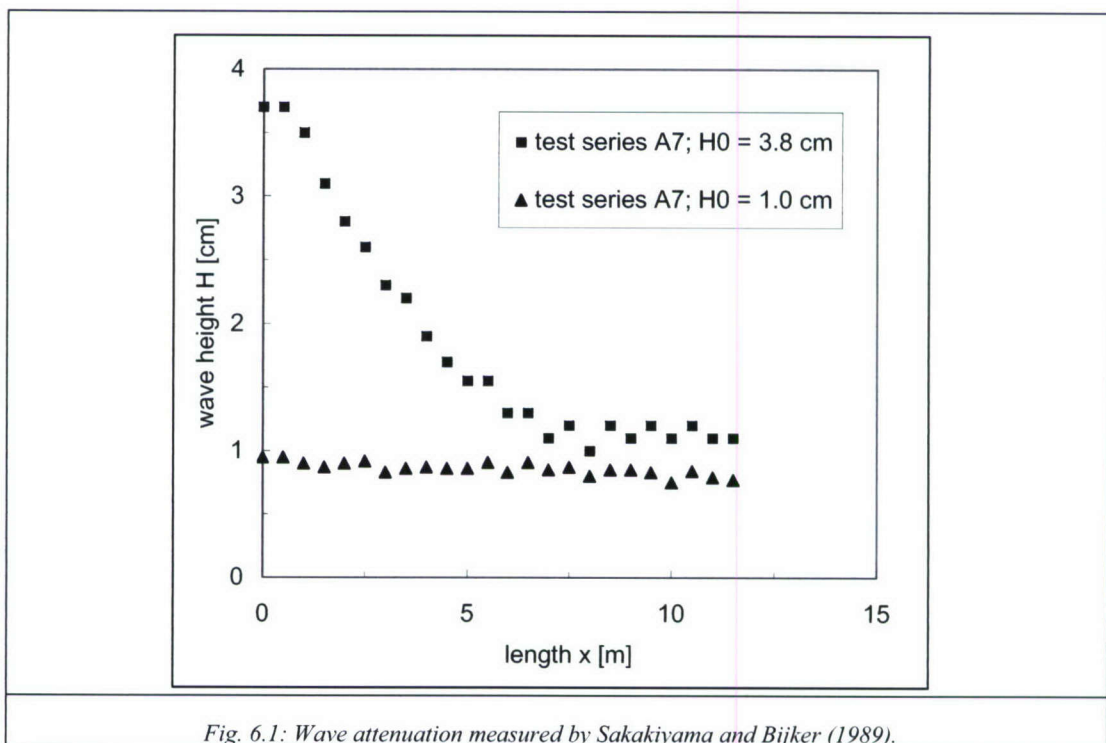
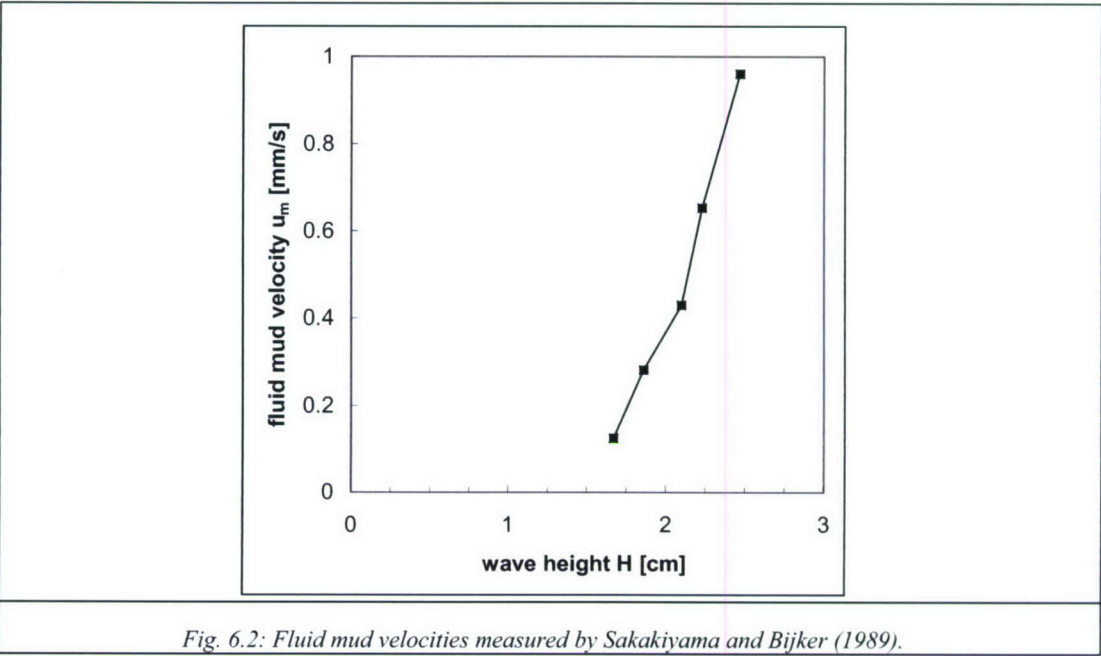


Fig. 6.1: Wave attenuation measured by Sakakiyama and Bijker (1989).

When mobile, the velocity within the mud bed amounted to about 0.1 – 1 mm/s, which was measured at about $x = 3.5$ m. The vertical velocity profiles were very homogeneous with little vertical gradients.

Fig. 6.2 shows very little variation of mud velocity with wave height. This implies a balance between the wave-induced traction and friction (yield stress), where the traction is

a linear function of the dissipation rate and gradient in wave energy. The dissipation rate appears to be more or less constant along the flume over the section where waves are damped, e.g. Fig. 6.1.



The parameters describing Sakakiyama and Bijker’s series A experiment are given in Table 6.1.

Table 6.1

mud parameters in 2L FLUID MUD model (data after Sakakiyama and Bijker (1989)).

ρ_w [kg/m ³]	ρ_m [kg/m ³]	$\delta_{m,0}$ [m]	h_0 [m]	H [m]	T [s]	ν_m [m ² /s]	α
1000	1370	0.09	0.3	0.035	1.0	$(1 - 2) \cdot 10^{-2}$	1

Dus test som bestaat uit eerste 5 m van goot, conform Fig. 6.1. Narekenen van het hele experiment is zinnig als we ook rheologisch model hebben ontwikkeld.

Eerste serie numerieke experimenten:

The first series of numerical experiments to test the combined effects of fluid mud induced wave damping and wave-induced fluid mud transport is carried out on a horizontal or sloping bed with waves at perpendicular direction – this simulates a coast with cross-shore waves. This lay-out is sketched in Fig. 6.3.

We carry out two series of experiments, Series 1: now waves, series 2: with waves. In both series, the slope of the bed i is increased in small steps from 0 to 10^{-3} rad., and in both series there is no water flow in the upper layer. Moreover, erosion, entrainment, sedimentation and consolidation are not included. The entire length of the model amounts to 2.5 km, with 20 m horizontal resolution. The width of the model is set to 2 km, and the width of the fluid mud layer at 1 km. Table 6.2 gives an overview of the various parameters:

--

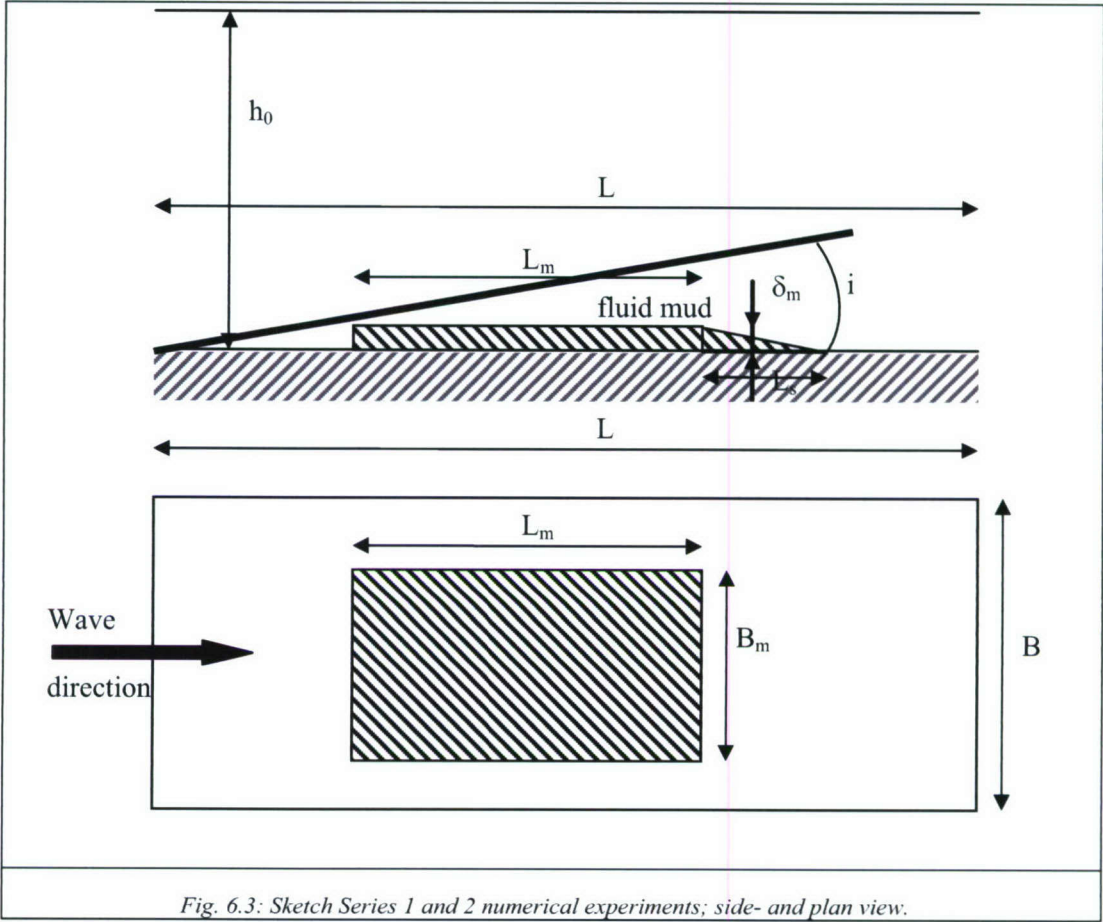


Fig. 6.3: Sketch Series 1 and 2 numerical experiments; side- and plan view.

Table 6.2
mud parameters in 2L FLUID MUD model for Series 1 & 2 experiments.

parameter	value	comments
h_0	5 m	largest depth in model – shallower “towards beach”
L	2500 m	
B	15,000 m	very wide because of wave spreading
δ_m	0.2 m	
L_m	60 (60) 600 m	to be varied
L_s	≥ 150 m	
B_m	600 m	symmetrical within overall domain
$\Delta x = \Delta y$	20 m	
Δt	2 min	based on internal celerity and $Cr = 5$; to be varied ($\Delta t = 0.5; 1; 5; 10$ min)
i	$0 (0.2 \cdot 10^{-3}) 10^{-3}$ rad	to be varied
H_s	2.0 m	
T	8 s	
ρ_w	1000 kg/m^3	
ρ_m	1370 kg/m^3	
ν_m	$1 \cdot 10^{-2} \text{ m}^2/\text{s}$	
τ_B	1 Pa	
λ	0.02	corresponds to $C \approx 60 \text{ m}^{1/2}/\text{s}$

The time step follows from the internal wave speed $c_i = \sqrt{(\rho_m - \rho_w) \varepsilon g \delta_m / \rho_w}$ and a Courant number not larger than about 5. Hence, $\Delta t \leq 5 \Delta x / c_i$, i.e. 117 s for the values of Table 6.2. Thus Δt is set to 2 minutes as a reference.

The configuration of Fig. 6.3 needs some refinement, as the density gradient at the edges of the fluid mud is too large to remain stable conditions in case of even a horizontal bed. Hence, edges as sketched in Fig. 6.3 should be added. Their length can be deduced from the balance between density gradient and bed shear stress (equ. (3.5)):

$$\frac{g \Delta \rho}{\rho_m} \frac{\partial Z_m}{\partial x_i} - \frac{\tau_{z_m, i}}{\rho_m \delta} = 0 \quad (6.1)$$

This leads to $L_s \geq g \delta^2 \Delta \rho / \tau_B$, amounting to 147 m for the values of Table 6.2.

The wave length for these conditions amounts to about 32 m, hence the real wave number $k_r = 0.2 \text{ m}^{-1}$ and $kh_0 = 0.98$. We have chosen the conditions such that the imaginary wave number is near its maximum, estimated at $k_i \approx 0.001 \text{ m}^{-1}$. Hence, within 150 m, 95% of the wave energy is expected to be dissipated within the fluid mud layer.

The Bingham strength τ_B is chosen such that the fluid mud should start to slide downhill at a bed slope $i > 0.5 \cdot 10^{-3} \text{ rad}$.

What effect of waves can be expected? For waves perpendicular to the coast (in x-direction), $\theta = 0$, and the radiation stress in this direction for monochromatic waves amounts to

$$\tau_x = -\frac{\partial}{\partial x} (\rho g (2n - 1/2) E) = \frac{1}{8} \frac{\partial}{\partial x} (\rho g (n - 1/2) H_s^2) \approx \frac{\rho g}{8} \frac{dH_s^2}{dx} \quad (6.2)$$

As $2n - 0.5 = \mathbf{O}\{1\}$. We have selected the wave-mud conditions such that $\delta_m (\sigma/2\nu)^{0.5} = 0.2 \cdot (\pi/8/0.01)^{0.5} = 1.25$, which yields about maximum damping. As $H_s = H_{s,0} \exp\{-k_i x\}$, $dH_s^2/dx = -2k_i H_s^2$. Substitution in (6.2) and use of (3.42) yields:

$$\frac{\tau_{r,m,x}}{\rho_m \delta_m} = \frac{\hat{\eta}_2^2}{\rho_1 \hat{\eta}_1^2 \delta_m} \tau_{r,m,x} = \frac{g}{4 \delta_m} \frac{\hat{\eta}_2^2}{\hat{\eta}_1^2} k_i H_s^2 \quad (6.3)$$

From our SWAN simulations we found that $k_i \approx 0.5 \cdot 10^{-3} \text{ m}^{-1}$. Further, $\hat{\eta}_2^2 / \hat{\eta}_1^2 \approx 0.1$, and we find $\tau_{r,m,x} / \rho_m \delta_m \approx 0.6 \cdot 10^{-3} H_s^2$ ($= 0.0024$ for $H_s = 2 \text{ m}$). This acceleration is small compared to gravitational effects of the mud on a slope. For instance $\alpha = 0.001$ one finds $g \Delta \rho \alpha / \rho = 0.0036$. Only for waves with $H_s > 2.5 \text{ m}$, the radiation stresses will exceed the gravitational effects.

However, in that case, the Bingham strength is still working, and the difference between the radiation stresses and gravitational effects for the conditions under consideration will never be large enough to overcome the Bingham strength and move the fluid mud uphill. This implies that this is only possible when the mud is truly liquefied and has lost all its strength.

7 Application of wave-induced liquefaction

To be completed

8 References

- Alba, P.D., Seed, H.B., Chan, C.K., 1976, Sand liquefaction in large-scale simple shear tests, ASCE, Journal of Geotechnical Engineering Division, Vol 102 (GT9) 909-927.
- Allison, M.A. and M.T. Lee, 2004, Sediment exchange between the Amazon mud banks and shore-fringing mangroves in French Guiana, Marine Geology, 208, 193-203.
- Augustinus, P.G.E.F., 2004, The influence of the Trade Winds on the coastal development of the Guianas at various scale levels: a synthesis, Marine Geology, 208, 145-153.
- Booij, N., R.C. Ris and L.H. Holthuijsen, 1999, A third-generation wave model for coastal regions, Part I: Model description and validation, Journal of Geophysical Research, 104 (C4) 7649-7666.
- Chou, H.-T., 1989, Rheological response of cohesive sediments to water waves, PhD-dissertation, University of California, Berkeley, USA.
- Chou, H.-T., M.A. Foda and J.R. Hunt, 1993, Rheological response of cohesive sediments to oscillatory forcing, in: Coastal and Estuarine Studies, Vol 42, Nearshore and Estuarine Cohesive Sediment Transport, ed. A.J. Mehta, 126-147.
- Coussot, P., 1997, Mudflow rheology and dynamics, IAHR monograph series, Balkema, Rotterdam, pp 255.
- Dalrymple, R.A. and P.L. Liu, 1978, Waves over soft mud beds: a two-layer fluid mud model, Journal of Physical Oceanography, 8, 1121-1131.
- Delft Hydraulics Laboratory, 1962, Demerara coastal investigation; Report on siltation of Demerara Bar Channel and coastal erosion in British Guyana, Vol 2, Field survey and basic studies, The Netherlands.
- Delft Hydraulics Laboratory, 1974, Momentum and mass transfer in stratified flows, Report R880.
- De Wit, P.J., 1995, Liquefaction of cohesive sediment by waves, PhD-dissertation, Delft University of Technology, The Netherlands.
- De Wit, P.J. and C. Kranenburg, 1997, On the liquefaction and erosion of mud due to waves and current, in: Cohesive Sediments, ed. N. Burt, R. Parker and J. Watts, John Wiley & Sons, 331-340.
- Dingemans, M.W., 1997, Water wave propagation over uneven bottoms; Part I & II, World Scientific, Singapore.
- Foda, M.A. and S.-Y. Tzang, 1994, Resonant waves of silty soil by water waves, Journal of Geophysical Research, 99 (C10) 20,463-20,475.
- Foda, M.A., J.R. Hunt and H.-T. Chou, 1993, A nonlinear model for the fluidization of marine mud by waves, Journal of Geophysical Research, 16 (2) 7039-7047.
- Gade, H.G., 1958, Effects of a non-rigid, impermeable bottom on plane surface waves in shallow water, Journal of Marine Research, 16 (2) 61-82.
- Golden, S.P., J.W. Godwin and A.D. Olal, 1982, The dependence of the elastic properties of clay dispersions on the mode of interaction between the particles, Transactions and Journal of the British Ceramic Society, 81 (3) 84-87.
- Groeneweg, J., 1999, Wave-current interactions in a Lagrangean mean formulation, PhD-thesis, Delft University of Technology, Department of Civil Engineering and Geosciences.
- Healy, T., Y. Wang and J.-A. Healy, 2002, Muddy coasts of the world: Processes, Deposits and Function, Elsevier, Proceedings in Marine Science No 4, 542 pp.
- Jiang, L. and Z. Zhao, 1989, Viscous damping of solitary waves over fluid-mud beds, ASCE, Journal of Waterways, Port, Coastal and Ocean Engineering, 115 (3) 345-362.
- Jiang, F., 1993, Bottom mud mass transport due to water waves, PhD-thesis, University of Florida, Gainesville, Florida, USA.
- Kurup, 1972, Littoral currents in relation to the mud bank formation along the coast of Kerala, Mahasagar, Bulletin of the National Institute of Oceanography, 5 (3).

- Lambe, T.W. and R.V. Whitman, 1979, *Soil Mechanics*, SI Version, John Wiley and Sons, New York, pp 553.
- Lindenberg, J., L.C. Van Rijn and J.C. Winterwerp, Some experiments on wave-induced liquefaction of soft cohesive soils, *Journal of Coastal Research*, 5, 127-138.
- Liu, P.L.-F., 1973, Damping of water waves over porous bed, *ASCE, Journal of the Hydraulic Division*, 92 (12) 2263-2271.
- Liu, K. and C.C. Mei, 1989, Effects of wave-induced friction on a muddy seabed modelled as a Bingham-plastic fluid, *Journal of Coastal Research*, 5 (4) 777-789.
- Longuet-Higgins, M.S., 1953, Mass transport in water waves, *Philosophical Transactions of the Royal Society of London, A* (903) 535-581.
- Longuet-Higgins, M.S., 1958, The mechanics of the boundary-layer near the bottom in a progressive wave, in: *Proceedings of the 6th Conference on Coastal Engineering*, Gainesville, Florida, ed. J.W. Johnson, Council on Wave Research; The Engineering Foundation, 184-193.
- Maa, P.-Y., 1986, Erosion of soft mud beds by waves, PhD-dissertation, University of Florida, Coastal and Oceanographic Engineering Department, Gainesville, Florida, USA, rep. UFL/COEL-TR-059.
- Maa, P.-Y. and A.J. Mehta, 1990, Soft mud response to water waves, *ASCE, Journal of Waterways, Port, Coastal and Ocean Engineering*, 116 (5) 634-650.
- MacPherson, H., 1980, The attenuation of water wave over a non-rigid bed, *Journal of Fluid Mechanics*, 97 (4) 721-742.
- Mallard, W.W., Dalrymple, R.A., 1977, Water waves propagating over a deformable bottom, *Proceedings of the 9th Offshore Technology Conference*, Houston, TX, Vol 3, 141-146.
- Malvern, L.E., 1969, *Introduction to the Mechanics of a Continuous Medium*, Prentice-Hall, Series in Engineering of the Physical Sciences, New Jersey.
- McDougal, W.G., Y.T. Tsai, P.-F. Liu, E.C. Clukey, 1989, Wave-induced pore water pressure accumulation in marine soils, *Journal Offshore Mechanics and Arctic Engineering*, ASME, 111, 1-11.
- Mei, C.C. and K.F. Liu, 1987, A Bingham plastic model for a muddy seabed under long waves, *Journal of Geophysical Research*, 94 (C13) 14,581-14,594.
- Mei, C.C., 1989, *Applied dynamics of ocean surface waves*, World Scientific.
- Mehta, A.J. 1996, Interaction between fluid mud and water waves, in: *Environmental Hydraulics*, ed. V.P. Singh and W.H. Hager, Kluwer Academic Publishers, The Netherlands, 153-187.
- Moore, F., 1959, The rheology of ceramic slips and bodies, *Transactions of the British Ceramic Society*, 58, 470-494.
- NEDECO, 1972, Report on sea defense studies of British Guyana, NEDECO, The Hague, The Netherlands.
- Phillips, O.M., 1977, *The dynamics of the upper ocean*, Cambridge University Press.
- Rodriguez, H.N., 2000, Mud bottom evolution at open coasts, PhD-dissertation, University of Florida, Coastal and Oceanographic Engineering Department, Florida, USA.
- Sakakiyama, T., E.W. Bijker, 1989, Mass transport velocity in mud layer due to progressive water waves, *ASCE, Journal of the Waterway, Port, Coastal, and Ocean Engineering*, 115 (5) 614-633.
- Sheremet, A., G.W. Stone, 2003, Observations of nearshore wave dissipation over muddy sea beds, *Journal of Geophysical Research*, 108 (C11), 21-1-21-11.
- Soulsby, R.L., S. Clarke, 2005, Bed shear-stresses under combined waves and currents on smooth and rough beds, HR Wallingford, Report TR 137.
- Spierenburg, S.E.J., 1987, Seabed response to water waves, PhD-dissertation, Delft University of Technology, The Netherlands.
- Stelling G.S., Kernkamp, H.W.J. and Laguzzi, M.M., 1998, "Delft Flooding System: a powerful tool for inundation assessment based upon a positive flow simulation", in *Hydro-informatics'98*, ed. by Babovic & Larsen, Balkema, Rotterdam, pp 449-460.

- Sumer, B.M., J. Fredsøe, 2002, The mechanics of scour in the marine environment, World Scientific, Advanced Series on Ocean Engineering, Vol. 17.
- Toorman, E.A., 1997, Modelling the thixotropic behaviour of dense cohesive sediment suspensions, *Rheologica Acta*, 36, 56-65.
- Tsuruya, H., S. Nakano, J. Takahama, 1987, Interaction between surface waves and a multi-layered mud bed, Report of the Port and Harbour Research Institute, Japan, 26 (5) 137-173.
- Tubman, M.W., Suhayda, J.N., 1976, Wave action and bottom movements in fine sediments, Proc. 15th ASCE conference, 1168-1183.
- Van Kesteren, W.G.M., Cornelisse, J.M., 1995, Modeling of the behavior of natural mud beds under cyclical or wave loading, Rijkswaterstaat and Delft Hydraulics, Research on Cohesive Sediment, Report 50.
- Van Kesteren, W.G.M., 2000, Slope stability analysis Orange River mouth, WL | Delft Hydraulics, Report Z2739.
- Verbeek, H. and J.M. Cornelisse, 1997, Erosion and liquefaction of natural mud under surface waves, in: *Cohesive Sediments*, ed. N. Burt, R. Parker and J. Watts, John Wiley & Sons, 353-364.
- Walstra, D.J.R., D.A. Roelvink and J. Groeneweg, 2000, Calculation of wave-driven currents in 3D mean flow model, *****
- Wang, Z.B. and J.C. Winterwerp, 1992, Transport of Fluid Mud, Numerical modeling with a two-layer system – research documentation, Report Z163.
- Wells, J.T. and J.M. Coleman, 1981, Physical processes and fine-grained sediment dynamics, coast of Surinam, South America, *Journal of Sedimentary Petrology*, 1053-1068.
- Wells, J.T. and G.P. Kemp, 1986, Interaction of surface waves and cohesive sediments: field observations and geologic significance, in: *Lecture Notes on Coastal and Estuarine Studies*, Vol 14, *Estuarine Cohesive Sediment Dynamics*, ed. A.J. Mehta, 43-65.
- Winterwerp, J.C., Z.B. Wang, J.A.Th.M. van Kester, J.F. Verweij, 2003, On the far-field impact of Water Injection Dredging, ICE/IAHR, Water and Maritime Engineering, Vol 154, Issue 4, pp 285-296.
- Winterwerp, J.C. and W.G.M. Van Kesteren, 2004, An introduction to the physical processes of cohesive sediment in the marine environment, Elsevier, *Developments in Sedimentology*, 56.
- Yamamoto, T., H.L. Koning, H. Sellmeijer and E. Van Hijum, 1978, On the response of a poro-elastic bed to water waves, *Journal of Fluid Mechanics*, 87 (1) 193-206.
- Yamamoto, T. and S. Takahashi, 1985, Wave damping by soil motion, ASCE, *Journal of the Waterway, Port, Coastal and Ocean Engineering*, 111 (1) 62-77.
- Zijlema, M. and A.J. van der Westhuijsen, 2005, On convergence behaviour and numerical accuracy in stationary in stationary SWAN simulations of nearshore wind wave spectra, *Coastal Engineering*, 52, 237-265.

A Appendix: List of symbols

A	wave semi-orbital excursion
a	aggregation coefficient in rate of flocculation equation
b	break-up coefficient in rate of flocculation equation
C_s	coefficient in entrainment model
C_σ	coefficient in entrainment model
c	sediment concentration by mass in upper layer
c	cohesion
c_0	cohesion at fully flocculated conditions
c	wave celerity
c_g	group velocity
c_m	sediment concentration by mass in fluid mud layer
c_v	consolidation coefficient
D	horizontal dispersion coefficient
D_{50}	median floc size
D_{ij}	rate of deformation tensor
D_m	settling from upper layer
E	total wave energy
E'	wave energy density
E_b	erosion consolidated bed
E_m	entrainment rate
ϵ_{ijk}	permutator: $\epsilon = 1/-1$ for cyclical/anti-cyclical i, j, k , otherwise $\epsilon = 0$.
F_i	wave-induced traction on fluid mud (streaming)
f	Coriolis parameter
f_{ws}	friction coefficient for waves
g	gravity
H	wave height
h	thickness of upper layer (\approx water depth)
h_0	initial thickness of upper layer
K_0	coefficient of lateral stress
K_k	permeability coefficient
K_p	effective stress coefficient
k	permeability
k	wave number
k_i	imaginary part wave number (wave damping)
k_r	real part wave number
k_λ	coefficient in friction coefficient
k_1	coefficient in erosion formula
k_2	coefficient in formula for critical shear stress
M_E	erosion parameter
N	wave action density
N	number of wave cycles during liquefaction
N_ℓ	number of wave cycles at liquefaction
n_f	fractal dimension
PI	plasticity index
P_w	wave-induced stresses on the seabed

p	pressure
p	isotropic stress
p_0	initial isotropic stress (i.e. prior to liquefaction)
p_w	amplitude wave-induced stresses on the seabed
\hat{Q}	deviatoric stress integrated over fluid mud layer thickness
q	deviatoric stress
\hat{q}	amplitude deviatoric stress
R	complex relative wave number
Re	Reynolds number
Ri^*	bulk Richardson number
S	salinity
S	switch function: $S(x) = x$ for $x > 0$
$S'_{b,m}$	fluid mud induced wave dissipation
T_{ij}	stress tensor
t	time
U_i	depth-mean velocity in upper layer
u	velocity of upper layer in x-direction
u_E	Eulerian velocity
u_L	GLM velocity (Generalized Lagrangean Mean)
u_S	stokes drift
u_{orb}	orbital wave motion
u^*	shear velocity of main flow
u^*_{*f}	shear velocity by main flow
$u^*_{*,m}$	shear velocity at water-mud interface
$u^*_{*,w}$	shear velocity by waves
u_m	velocity of fluid mud layer in x-direction
v	flow velocity in y-direction
v_m	velocity of fluid mud layer in y-direction
W_c	consolidation velocity
W_s	settling velocity
W	vertical velocity
w_s	vertical velocity of solids
x	longitudinal co-ordinate
y	longitudinal co-ordinate
Z_b	elevation of consolidated bed with respect to reference level
Z_m	elevation of water-mud interface with respect to reference level
Z_s	elevation of water surface with respect to reference level
Π_D	second invariant of rate of deformation tensor
α	calibration coefficient fluid mud induced dissipation
δ	thickness fluid mud layer
δ_{max}	maximal (user-defined) thickness fluid mud layer
δ_0	initial thickness fluid mud layer
$\Delta\rho$	density difference over water-mud interface
Γ_T	turbulent eddy diffusivity
$\dot{\gamma}$	shear rate
η_1	elevation of water surface
η_2	elevation of interface

θ	wave direction
λ	friction coefficient
λg	complex Stokes number
λ_s	structure parameter
μ	mud viscosity
μ'	mud viscosity parameter
μ_∞	residual mud viscosity at fully deflocculated state
ν	kinematic viscosity
ν_m	viscosity mud layer
ν_T	turbulent eddy viscosity
ρ	fluid density of upper layer (taking into account the effect of salinity)
ρ_{dry}	dry bed density (mass concentration) of fluid mud layer
ρ_m	bulk density of fluid mud layer
σ	wave number (frequency)
σ	normal and/or principal stress
σ_{zz}^{sk}	vertical effective stress
τ	shear stress
τ_b	bed shear stress
τ_B	Bingham strength
τ'_B	Bingham strength parameter
$\tau_{B,\infty}$	residual Bingham strength at fully deflocculated state
$\tau_{c,e}$	critical shear stress for erosion
τ_d	critical shear stress for deposition
τ_Z	shear stress at level Z (i.e. water surface, interface and base of mud layer)
ν	Poisson ratio
ϕ	angel of repose / internal friction
ϕ	volumetric concentration
ϕ	phase angle water elevation and flow velocity of surface waves
ϕ_0	angel of repose / internal friction at fully flocculated state
ϕ'	phase angle between surface and internal waves

B .Appendix: Table of parameters

symbol	description		unit	dim.	user input	default value	computed in	used in
A	wave semi-orbital excursion		m					
a	aggregation coefficient in rate of flocculation equation		1/s	const	yes	**		rheology
b	break-up coefficient in rate of flocculation equation		-	const	yes	**		rheology
c	sediment concentration by mass in upper layer		kg/m ³					
c	cohesion		Pa					
c_0	cohesion at fully flocculated conditions		Pa					
c	wave celerity surface wave		m/s	x,y,t			SWAN	lower layer
c_m	wave celerity fluid mud – water interface		m/s	x,y,t			lower layer	lower layer
c_g	group velocity		m/s					
c_m	sediment concentration by mass in fluid mud layer		kg/m ³	const	yes	80		lower layer, SWAN
c_v	consolidation coefficient		m ² /s	const	yes	10 ⁻⁸		lower layer
D	horizontal dispersion coefficient		m ² /s					
D_{50}	median floc size		m					
D_{ij}	rate of deformation tensor		1/s					
D_m	deposition rate from upper layer		kg/m ² /s	x,y,t			upper layer	lower layer upper layer
E	total wave energy		J/m ²	x,y,t			SWAN	lower layer
E'	wave energy density		W/m ²	x,y,t			SWAN	SWAN
E_b	erosion rate consolidated bed		kg/m ² /s	x,y,t			lower layer	lower layer
E_b	erosion rate consolidated bed		kg/m ² /s	x,y,t			upper layer	upper layer
E_m	entrainment rate		kg/m ² /s	x,y,t			lower layer	lower layer upper layer
e_{ijk}	permutator: e = 1/-1 for cyclical/anti-cyclical i, j, k, otherwise e = 0.		-					
F_i	wave-induced traction on fluid mud (streaming)		Pa	x,y,t			lower layer	lower layer
f	Coriolis parameter		-					

f_s	friction coefficient for flow		-	const	yes	$4 \cdot 10^{-4}$	computed in	lower layer upper layer
symbol	description		unit	dim.	user input	default value		used in
f_s	friction coefficient for flow		-	const	yes	$4 \cdot 10^{-4}$		lower layer upper layer
f_{ws}	friction coefficient for waves		-	const	yes	0.005		lower layer upper layer
g	gravity		m/s^2					
H	wave height		m	x,y,t			SWAN	liquefaction
h	thickness of upper layer (\approx water depth)		m					
h_0	mean thickness of upper layer		m					
K_0	coefficient of lateral stress		-	const		0.5	rheology	liquefaction
K_k	permeability coefficient		m/s	const	yes	10^{-14}		lower layer
K_p	effective stress coefficient		Pa	const	yes	10^9		lower layer
k	permeability		m/s					
k	wave number		1/m	x,y,t			SWAN	liquefaction
k_i	imaginary part wave number (wave damping)		1/m					
k_r	real part wave number		1/m					
k_λ	coefficient in friction coefficient		-	const	yes	64		rheology
k_l	coefficient in erosion formula		-	const	yes	1		lower layer upper layer
k_2	coefficient in formula for critical shear stress		-	const	yes	1		lower layer upper layer
M_E	erosion parameter		s/m	x,y,t			lower layer	lower layer
M_E	erosion parameter		s/m	x,y,t			upper layer	upper layer
N	wave action density		J/m ²					
N	number of wave cycles during liquefaction		-					
N_l	number of wave cycles at liquefaction		-					
n_f	fractal dimension		-	const	yes	2.7		lower layer
PI	plasticity index		%	const	yes	80		lower layer

P_w	wave-induced stresses on the seabed		Pa							
p	pressure		Pa							
symbol	description		unit	dim.	user input	default value	computed in	used in		
p	isotropic stress		Pa							
p_0	initial isotropic stress (i.e. prior to liquefaction)		Pa	x,y,t			liquefaction			liquefaction
p_w	amplitude wave-induced stresses on the seabed		Pa	x,y,t			liquefaction			liquefaction
$\left(\frac{\hat{q}}{p_0}\right)_{crit}$	critical cyclical stress ratio		Pa	const	yes		liquefaction			liquefaction
\hat{Q}	deviatoric stress integrated over fluid mud layer thickness		Pa	x,y,t			liquefaction			rheology
q	deviatoric stress		Pa							
\hat{q}	amplitude deviatoric stress		Pa	x,y,t			liquefaction			liquefaction
R	complex relative wave number		s ² /m ²							
Re	Reynolds number		-							
Ri*	bulk Richardson number		-	x,y,t			lower layer			lower layer
S	salinity		ppt							
S	switch function: $S(x) = x$ for $x > 0$									
$S'_{h,m}$	fluid mud induced wave dissipation		W/m ²	x,y,t			SWAN			SWAN, lower layer
T_{ij}	stress tensor		Pa							
t	time		s							
U_i	depth-mean velocity in upper layer		m/s	x,y,t			upper layer			lower layer
U_{orb}	orbital wave motion at bed		m/s	??						
u	velocity of upper layer in x-direction		m/s							
u_E	Eulerian velocity		m/s	x,y,t			lower layer			lower layer rheology
u_m^L	GLM velocity (Generalized Lagrangean Mean) in x-direction		m/s	x,y,t			lower layer			lower layer
u_S	stokes drift		m/s							
u_*	shear velocity		m/s	x,y,t			lower layer			lower layer

u_{*f}	shear velocity by main flow at water-mud interface	m/s	x,y,t				lower layer	lower layer
u_{*m}	shear velocity at bed-fluid mud interface	m/s	x,y,t				lower layer	lower layer
symbol	description	unit	dim.	user input	default value	computed in	used in	
u_{*w}	shear velocity by waves at water-mud interface	m/s	x,y,t			lower layer	lower layer	
u_m	velocity of fluid mud layer in x-direction	m/s						
v	flow velocity in y-direction	m/s						
v_m	velocity of fluid mud layer in y -direction	m/s						
v_m^L	GLM velocity (Generalized Lagrangean Mean) in y-direction	m/s	x,y,t			lower layer	lower layer, rheology	
W_c	consolidation rate lower layer	kg/m ² /s	x,y,t			lower layer	lower layer	
W_s	settling velocity	m/s						
w	vertical velocity	m/s						
w_s	vertical velocity of solids	m/s						
x	longitudinal co-ordinate	m						
y	longitudinal co-ordinate	m						
Z_b	elevation of consolidated bed with respect to reference level	m						
Z_m	elevation of water-mud interface with respect to reference level	m						
Z_s	elevation of water surface with respect to reference level	m						
Π_D	second invariant of rate of deformation tensor	1/s ²	x,y,t			rheology	rheology	
α	calibration coefficient fluid mud induced dissipation	-	const	yes				
δ	thickness fluid mud layer	m						
δ_{max}	maximal (user-defined) thickness fluid mud layer	m	x,y	yes			liquefaction	
$\delta_{m,0}$	mean thickness fluid mud layer	m	x,y			liquefaction	SWAN, lower layer	
$\Delta\rho$	density difference over water-mud interface	kg/m ³						
Γ_T	turbulent eddy diffusivity	m ² /s						
$\dot{\gamma}$	shear rate	1/s						
η_l	elevation of water surface	m						

$\hat{\eta}_1$	amplitude elevation of water surface	m	x,y,t						
η_2	elevation of interface	m							
symbol	description	unit	dim.	user input	default value	computed in			lower layer
$\hat{\eta}_2$	elevation of water surface	m	x,y,t			SWAN			lower layer
θ	wave direction	deg							
λ	friction coefficient	-	const			rheology			lower layer
λg	complex Stokes number	1/m							
λ_s	structure parameter	-	x,y,t			rheology			rheology
μ	mud viscosity	Pa·s	x,y,t			rheology			rheology, lower layer
μ'	mud viscosity parameter	Pa·s	const	yes	10^{-3}				
μ_c	residual mud viscosity at fully deflocculated state	Pa·s	const	yes	10^{-5}				
ν	kinematic viscosity	m ² /s							
ν_m	viscosity mud layer	m ² /s	x,y,t			rheology			rheology, lower layer
ν_T	turbulent eddy viscosity	m ² /s							
ρ	fluid density of upper layer (taking into account the effect of salinity)	kg/m ³							
ρ_{dry}	dry bed density (mass concentration) of fluid mud layer or consolidated bed	kg/m ³							
ρ_m	bulk density of fluid mud layer	kg/m ³	const			lower layer			SWAN, lower layer
ρ_s	bulk density of fluid mud layer	kg/m ³	const	yes	2650				
ρ_w	bulk density of fluid mud layer	kg/m ³	const	yes	1020				
σ	wave number (frequency)	1/s							
σ	normal and/or principal stress	Pa							
σ_{zz}^{sk}	vertical effective stress	Pa							
τ	shear stress	Pa							
τ_b	bed shear stress	Pa							
τ_B	Bingham strength	Pa	x,y,t			rheology			rheology,

	Bingham strength parameter		Pa	const	yes	1		lower layer rheology
τ'_B			unit	dim.	user input	default value	computed in	
symbol	description							used in
$\tau_{B,\infty}$	residual Bingham strength at fully deflocculated state		Pa	const	yes	5		rheology
$\tau_{c,e}$	critical shear stress for erosion		Pa	const			lower layer	lower layer
τ_Z	shear stress at level Z (i.e. water surface, interface and base of mud layer)		Pa					
ν	Poison ratio		-					
ϕ	volumetric concentration		-					
$\phi_{s,0}$	volumetric concentration prior to swelling		-	const			lower layer, upper layer SWAN	lower layer, upper layer SWAN
ϕ'	phase angle between surface and internal waves		deg				rheology	rheology
φ	angel of repose / internal friction		deg					
φ_0	angel of repose / internal friction		deg	const	yes	30		rheology
ψ	phase angle water elevation and flow velocity of surface waves		deg	x,y,t			SWAN	lower layer